Gas sensing properties of YMnO3 based materials for the detection of NOx and CO

Gas sensing properties of $YMnO_3$ based materials for the detection of NO_x and CO

Tommaso Addabbo[1], Francesco Bertocci[1], Ada Fort[1], Michele Gregorkiewitz[2], Marco Mugnaini[1], Roberto Spinicci[1], Valerio Vignoli[1].

[1]Dipartimento di Ingegneria dell'Informazione e Scienze Matematiche – Università di Siena – via Roma 56 -53100 Siena

[2]Dipartimento di Scienze Fisiche, della Terra e dell'Ambiente – Università di Siena – via Laterina 8 -53100 Siena

Highlights

- This paper studies the gas sensing properties of hexagonal $YMnO_3$ produced by gel combustion in stoichiometric, defective and doped form with CO and NO_x.
- All the tested materials have a fast reversible response to NO_2 at the optimum temperatures close to 180 °C. As far as CO detection is concerned, materials impregnated with Pd have the best performance both in terms of speed and of sensitivity, with an optimum temperature of 300 °C.
- The results presented show that for $YMnO_3$ the chemistry of the defects is fundamental to determine the gas sensing properties in terms of speed and magnitude of the response.
- The experimental results, supported by a sensor model, seem to indicate that, besides the oxygen chemisorption, the direct adsorption of the target gases at the material surface plays a fundamental role in gas sensing.

Abstract

This paper deals with chemoresistive behavior of hexagonal $YMnO_3$ produced by gel combustion. Stoichiometric, defective and doped compositions were studied and both reducing (CO) and oxidizing test gases (NO_x) were used. The materials were characterized by means of X-ray diffraction, CO conversion tests, and oxygen temperature programmable desorption (TPD) and temperature programmable reduction (TPR) with H_2. Experiments indicate that, besides the oxygen chemisorption, the direct adsorption of the target gases at the material surface plays an important role in resistive gas sensing. A model based on these assumptions was developed and excellently fits the transient response of the sensors under test to NO_2 in the absence of oxygen.

All the tested materials behave as p-type semiconductors and have a fast reversible response to NO_2 which is optimum at temperatures close to 180 °C (30% @10 ppm NO_2, after about 1 min). In particular, it was found that the best sensor performance in NO_2 detection is obtained with defective materials in terms of response, while an interesting trade-off between temperature response and gas response is obtained with Pd doped materials. Regarding CO detection, materials impregnated with Pd showed the best performance both in terms of speed and of response, with an optimum temperature of 300 °C.

Keywords: Metal oxide gas sensors; Hexagonal $YMnO_3$; Chemoresistive sensor materials; p-type semiconductors; Gas sensor modeling.

1. Introduction

A great deal of research efforts has been directed toward the development of miniaturized gas-sensing devices particularly for the detection of toxic gases such as CO and NO_x, due to a great interest in many different fields, from environmental monitoring to combustion control in industrial plants and automotive applications. Though several devices are available for gas detection, solid state metal oxide sensors offer many advantages among which low cost and large response to the target gases [1]. Many binary oxides in a variety of versions of micro- or nanostructures have been extensively studied, such as SnO_2, CuO, ZnO, Fe_2O_3 for CO sensing, and SnO_2, In_2O_3, WO_3 and ZnO for detection of NO_x [2]. Many of these materials, both in the pure form and in combination with dopants or additives, proved to have large responses, and reasonable response and recovery times. Nevertheless, there is still a strong demand for novel, high performance and reliable materials/devices for advanced applications ensuring improved performance, especially in terms of selectivity and stability.

Much work in this respect has been focused on ternary oxide semiconductors, especially perovskite-type compounds, which can show a large chemical reactivity and a stable behavior. Moreover, the structure of many ternary oxides semiconductor presents a remarkable flexibility and in many cases can tolerate significant isomorphic substitutions and non-stoichiometry. Since the physical and chemical properties of such compounds heavily depend on the defect chemistry,

these materials might be adjusted or tailored to the specific application [3]. For instance, a small change in oxygen stoichiometry can induce large differences in electronic conduction, surface redox behavior, heterogeneous catalysis [4] and gas selectivity.

In this context, the development of both 'high temperature' (electrochemical) and 'low temperature' (chemoresistive) ternary oxide gas sensors has been explored [5]. Electrochemical sensors operate at temperatures higher than 350°C, and the oxide can be an electrode and/or the solid state ionic conductor. The gas detection is based on the oxidation/reduction of the target gas at one electrode involving also electrolyte bulk ionic species. On the other hand, chemoresistors operate at temperatures below 400°C and behave as electronic conductors: the chemical reactions affecting conductivity are supposed to be reversible chemisorptions taking place at the surface of the material without a direct involvement of lattice atoms.

Generally speaking, chemoresistors are easy to manufacture (if compared with electrochemical sensors), and present a response, in terms of relative resistance variation, that can be larger, also at temperatures much lower than it happens for electrochemical sensors. On the other hand, with respect to selectivity, the performance of chemoresistors is in general lower that the performance of electrochemical sensors [6-7].

Many ternary oxides have been proposed as the electrode material for 'high temperature' electrochemical sensors (Fergus [6] reviewed this topic). On the other hand, their application as chemoresistors has been investigated more recently, but in any case several types of ternary oxide, mainly perovskite, sensors have been proposed, which are easy to manufacture, have good performance, satisfactory response, reduced dependence on environmental conditions (humidity) and satisfactory stability [7-8]. For instance, $LaCoO_3$ was proposed for CO detection, compositions based on $LnFeO_3$ (Ln=La, Sm, Nd) for the detection of organic compounds or O_3, NO_2 and CO [3][8-10], and recently, $YCoO_3$ for the detection of NO_x [11].

In this paper we study the chemoresistive behavior of hexagonal $YMnO_3$ produced by gel combustion both toward reducing (CO) and oxidizing gases (NO_2).

This material has already received much attention due to its magnetic and ferroelectric properties [4][12-13], but its gas sensing properties are still scarcely studied, even if the large number of possible oxidation states of Mn induces to expect a highly reactive surface.

$YMnO_3$, that can have both a tetragonal or, more frequently, a hexagonal layer structure, based on MnO_5 bipyramids [14-17], is a semiconductor with a band gap between 1.28 eV and 1.55 eV

[18-19]. As many other transition ternary metal oxides it is expected to have a native p-type behavior related to the favored formation of acceptor states during the preparation, both metal vacancies or oxygen excess, depending on the materials and on the preparation route. Cation deficient composition could take place because Mn^{4+} ions are stable in oxides, and cation vacancies can be created through isomorphous substitution $Mn^{3+}_4 = Mn^{4+}_3 \square$ (where $\square$ indicates a Mn vacancy) for charge compensation. Actually, as far as oxygen stoichiometry is concerned, the formula should be written $YMnO_{3+\delta}$ and both over- ($\delta > 0$) and under- ($\delta < 0$) stoichiometry of oxygen is found in the literature [4][20-22].
Following an approach used in a previous work aimed at the characterization of $YCoO_3$ [11], the material is studied in its stoichiometric form and in non stoichiometric or doped derivatives.

Defective materials are prepared in the attempt of enhancing the response to NO_x. In fact, based on the hypothesis proposed in other studies for other materials with RBO_3 composition (R rare earth, B transition metal), the sensitivity toward oxidizing gases, and in particular NO_2, is expected to increase when increasing the B^{4+}/B^{3+} ratio on the surface [3].
To favor CO detection, on the other hand, we modified the material with the addition of Pd that acts as a catalyst for CO oxidation, but it must be remembered the catalytic activity toward the oxidation of CO can follow paths different from those involved in the conductimetric response, so the efficiency of Pd introduction has to be experimentally tested.

To deepen the study of the chemoresitive behavior of the analyzed materials, we correlated the results obtained through different kinds of characterization techniques, (structural characterization by X-ray diffraction, measurement of the efficiency of the conversion of CO into CO_2, TPD of oxygen, TPR with H_2, and finally resistance measurements). This has allowed us to formulate hypotheses about the influence of the structure of the material on its response, and about the nature of the chemical reactions that take place at the surface.

To validate some of these hypotheses, a model has been developed for the transient chemoresitive response in simple chemical conditions (presence of a single gas). We model the observed chemical responses using a model similar to others presented in the literature (see, for example, [23-26] and references therein).

2. Material and methods

2.1. Preparation of samples of nominal formula $YMnO_3$ and of derivative compositions

Equimolar amounts of the hydrates nitrates of Y and Mn were used. The two powders, mixed with a double amount of moles of citric acid were suitably dissolved in distilled water, adding ammonium nitrate (all reagents are Aldrich, purity > 99.9%).
The solution was heated to form a viscous sol which, before gelling, was transferred directly in the furnace at 600 °C where it remained 24 hours before raising the temperature up to 900 °C. In the furnace the gel bursts into flames after few seconds, producing a spongy powder, greenish - black coloured, very crumbly. This powder becomes black after the treatment at 900 °C and the particles are visibly fine.

With the aim to prepare defective compositions, $YMn_{1-x}O_3$ or $Y_{1-x}MnO_3$, the molar ratio in the reaction mixture was varied to 1:(1-x) or (1-x):1, with *x* in the range 0.01-0.1. Similarly, to obtain the doped compositions $YMn_{1-x}Pd_xO_3$, small quantities (x = 0.03 to 0.1) of Pd(II) nitrate or acetate were added to the mixture of Y and Mn nitrates, followed by the heating and calcination steps as above.

Impregnated products were prepared by soaking $YMnO_3$ in an aqueous solution of $Pd(NO_3)_2$ or $Pd(CH_3COO)_2$. The salts, kept dry under vacuum, were dissolved in distilled water or acetone, the solution added to the metal oxide powder in a mass ratio varying between 0.005 and 0.01, and the mixture was then dried in a muffle in a temperature range between
500 °C and 650 °C for 6 to 18 hours. These products are hereafter indicated with the name of the starting material followed by '+ X wt% Pd'.

The different materials studied in this work are listed in table I; each tested composition is indicated with a letter and with a nominal formula which is meant as a working designation maintained throughout the paper even if the presence of vacancies or Pd substitutions could not be ratified from structural characterization (see results section).

Table I about here

2.2. Characterization methods

For X-ray diffraction experiments, the powders were ground in an agate mortar to break agglomerates. Further grinding was not necessary considering the small grain size resulting from the synthesis procedure.

Diffraction patterns, with angles 2□ ranging from 3º to 85º, were obtained using a Panalytical X'pert powder diffractometer with Bragg-Brentano geometry, Ni-filtered CuKα radiation (λ1=1.540598, λ2=1.544418 Å) and an X'Celerator linear position sensitive detector.

The observed patterns were used in Rietveld refinements (program GSAS, [27]) to determine the modal composition of the powders and to assess possible changes of the unit cell parameters and the size of the crystalline domains. The number of refined overall parameters was therefore limited to a minimum (12 background coefficients and one correction term for the origin of the pattern), and instrumental parameters (peak broadening and asymmetry) have been fixed to values determined in separate experiments using standard samples. Starting parameters for the unit cells and the atom positions were taken from the literature for the main phase (hexagonal $YMnO_3$, van Aken et al. [28]) and identified impurities (Y_2O_3, Baldinozzi et al. [29]; orthorhombic $YMnO_3$, Okuyama et al. [30]; PdO, Waser et al. [31]; and Pd, Wyckoff [32]). During least-squares refinement, the atom parameters of the impurities (Y_2O_3, orthorhombic $YMnO_3$, Pd, PdO) were kept at their original values throughout but the unit cell parameters were allowed to refine for all major (>1 mass%) phases in the mixtures.

Catalytic activity, oxygen desorption, and surface reduction were studied by means of a continuous flow tubular reactor where 0.05 – 0.1 g of the prepared powder was placed, and the temperature could be controlled in the range 100 °C – 800 °C. Test gases were passed over the sample at a controlled and constant flow rate of 24 mL/min, and the outlet gas was analyzed by means of a Perkin Elmer Autosystem gas chromatograph equipped with hot wire detector and capillary columns.

The catalytic activity was investigated in the range 80 °C – 250 °C increasing the temperature stepwise. For CO conversion measurements, the samples were pretreated by heating at 450 °C in He + O_2 (20%) for 1 hour, and subsequently cooled to the reaction temperature (this procedure was repeated for each temperature step); the reaction was performed by injecting a mixture of He

+ CO (2 %) and O_2 (20%). The results are expressed in terms of CO conversion, i.e. the ratio of CO_2 concentration at the outlet to CO concentration at the inlet, in percentage.

Temperature programmed desorption (TPD) measurements were performed after pretreatment as before but cooling down to room temperature where the samples were kept under the same gas flow for 1 hour. After this time a flow of pure helium was fed in the reactor and the measurement started while the temperature was progressively increased at 8 °C/min.

For temperature programmed reduction (TPR) measurements the samples were pretreated in the same way as in TPD experiments. After conditioning at room temperature, a flow of He + H_2 (10%) was fed into the reactor and the measurement started while the temperature of the catalyst was progressively increased at 8 °C/min.

In order to assess the gas sensing properties, prototype gas sensors were realized by screen printing technique depositing a thick film obtained from the different prepared materials. A printable ink was obtained by mixing the metal oxide powders with an organic vehicle (dimethylphtalate), and by adding some percents of glass frit. The ink was deposited on the alumina substrate shown in Fig. 1, (width = 8mm, length =15 mm, thickness 0.2 mm), equipped with Ag electrodes, which also hosts a Pt temperature sensor and a heater on the backside. After film deposition the devices were fired up to 600 °C for some hours [33]. The morphology of the oxide powders and the thick films was analyzed by scanning electron microscopy (SEM).

Figure 1 about here

Resistance measurements were performed in a stainless steel test chamber under a constant gas flow of 200 mL/min. The characterization of the gas sensor response was obtained in terms of both temperature and concentration dependence through a fully automated measurement system [33]. The resistance was measured by applying a DC voltage lower than 1.5 V; in this voltage range the I-V behavior of the film is ohmic. The measurement circuit is described in detail in [33]. Sensors were tested with CO and NO_x mixtures in dry and humid air or nitrogen as carrier gases.

3. Experimental results and discussion: material structure and chemistry

3.1. Structural and morphologic characterization

The sol–gel self-combustion creates porous nanoparticle aggregates (Fig. 2) after thermally induced self-sustaining redox reactions between metal nitrates and reducing agents. The exothermic combustion with a rapid evolution of heat creates high crystallinity materials, and the gas release creates open pore structures with a large surface area [34]: these open pore networks are supposed to enhance gas diffusion. The pore network is fine, with pore size of about 50 nm and grain diameter of about 100 nm.

The surface area, measured by the Brunauer–Emmett–Teller (BET) analysis of the samples, is equal to 6.50 m^2/g. For free spherical particles with a diameter of 100 nm and density 5.0 g/cm^3 we expect a surface area of ~12 m^2/g, so the smaller observed value is obviously due to the agglomeration of grains in the gut-like morphology. In any case a beneficial feature of the prepared material is the smaller size of the crystallite that can lead to fast and enhanced gas responses [11].

Figure 2 about here

Powder X-ray Diffraction (PXRD) patterns (Fig. 3) have been obtained for the most representative materials (A, B, C, D) and show that all of them contain hexagonal $YMnO_3$ (JCPDS PDF card no. 25-1079) as the main phase, accompanied by 1-2 mass% of the orthorhombic (perovskite) $YMnO_3$ polymorph and variable amounts of yttria Y_2O_3 which are highest in B ($YMn_{0.9}O_3$). Palladium bearing samples (C, D) contain, in addition, small amounts of PdO and metallic Pd which increase with the amount of Pd present during synthesis (the same can, by analogy with earlier work [11], be assumed for impregnated samples where no diffraction patterns have been obtained).

Quantitative results obtained from Rietveld refinements are summarized in Table II. The most important variations refer to the modal composition of the powders. Ideally, defective and Pd substituted materials can be prepared by controlling the precursor molar ratios. If the effect of changing the molar ratios was actually limited to inducing metal vacancies or Pd substitution in $YMnO_3$, we would expect the diffraction pattern of hexagonal $YMnO_3$ throughout, allowing for minor adjustments in peak positions and intensities to account for the substitution of Mn by a vacancy or Pd. The actual scenario is different and we clearly recognize that both Y and Pd are present in separate phases. From modal compositions, in fact, it seems that the mass fractions of Y_2O_3 and Pd+PdO roughly reproduce the composition of the substrate as can be seen best in the

molar ratios which are near to the expected values of 1/9 = 0.11 and 2/9=0.22 for mixtures of the pure phases.

Another sensible variation can be seen in the unit cell parameters of hexagonal $YMnO_3$ where *a* increases steadily from the pure compound up to the defective composition $YMn_{0.9}O_3$ and *c* falls abruptly in material B (see the last column of Table II). This suggests that the "hexagonal $YMnO_3$" structure undergoes slight structural changes in response to its exact composition, mainly regarding the Y/Mn ratio or oxygen over/understoichiometry. In the literature it can be found, on the other hand, that the unit cell varies with grain size below a diameter of $t \approx 100$ nm ([16]) and, from the trends reported, a cell volume of 373.5(372.4) $Å^3$ would be expected for $t \approx$ 50(100) nm. From Rietveld refinement, we find cell volumes ranging from 372.8 to 374.3 $Å^3$ (Tab. II), within ≤0.8 $Å^3$ around 373.5 $Å^3$, while the grain size is $t \approx 50(5)$ nm throughout for all four samples. Note that this value, which refers to the coherent domain compares well with the grain size of 100 nm estimated in SEM: the visible grains are usually made up from some coherent domains, in our case gut-like agglomerates with a diameter down to about 50 nm (Fig. 2).

The scatter of values for the unit cell parameters can therefore not be ascribed to grain size. Slight differences in composition or defect chemistry might be at the origin but structural parameters give no hint to solve the problem. In particular, the refined Mn/Y ratio is close to 1 (1.002 to 1.03) for all four samples, and there is no change in the Mn-O and Y-O bond distances. Vacancies or substitutions at the metal sites can therefore not be directly proven. The only measurable variation refers to oxygen over/understoichiometry, with δ = 0.12, 0, -0.06 and -0.21 in $YMnO_{3+\delta}$ for $YMnO_3$, $YMn_{0.95}Pd_{0.05}O_3$, $YMn_{0.9}Pd_{0.1}O_3$ and $YMn_{0.9}O_3$, respectively (that is, materials A, D, C, B). Similar variations have indeed been observed [4][20-22], but their relation to unit cell and structure is still waiting for an explanation (significance of site occupation factor (SOF) refinement, reproducibility issues with flame combustion).

Resuming, our syntheses yielded essentially pure hexagonal $YMnO_{3+\delta}$ in all cases, with some indication for oxygen over/understoichiometry, accompanied by additional phases (Y_2O_3, PdO, Pd) which will be important for the discussion of chemical and sensor behavior. In this context, a comment should be made about the metastable orthorhombic $YMnO_3$ phase. Earlier work ([14-

16]) has pointed out that, at 1 bar and 700-960 ºC, an oxidizing agent (O_2, NO_3^-) is necessary during synthesis in order to get the orthorhombic phase, while the stable hexagonal polymorph is promoted by a reducing environment (see [21] for a possible explanation in terms of δ and of Goldschmidt and [35] tolerance factor). Accordingly, crystallization of the hexagonal phase takes place, either from an amorphous precursor or by transition from the orthorhombic polymorph, at temperatures ranging from 750 to 1000 ºC, depending on redox conditions and precursor materials ([14][16][36-37]). Temperatures beyond 1000 ºC will always yield the hexagonal phase and the orthorhombic material can only be obtained under considerable pressure (e.g. 1200 ºC, 55 kbar; [38]), as expected from its much smaller molar volume (56.40 instead of 62.13 $Å^3$ for hexagonal $YMnO_3$).

During flame combustion, temperature and redox conditions are difficult to define but, in our case, there is a considerable amount of citrate which acts as a reducing agent and the calcination temperature of 900 ºC is probably sufficient to explain the formation of almost pure hexagonal $YMnO_3$. It may, however, be assumed that such procedure cannot warrant an exact stoichiometry.

The high quality of these results is witnessed by low statistical indices (χ^2) and very low powder (Rp) and structure (RF2) residual errors. Similarly, comparison of the observed and calculated patterns (Fig. 3) shows excellent agreement except for some ripple due to peak asymmetry, a known issue with area detectors [39].

Figure 3 about here

Table II about here

3.2. CO conversion experiments

To further the study on CO sensing the catalytic activity in terms of CO oxidation of the prepared materials was tested, and the results are shown in Fig. 4.

As many researchers pointed out, the CO sensing can be related to the CO catalytic conversion, but the relationship between the two phenomena is not simple [11]. In fact, CO

conversion can follow different chemical reaction paths from those involved in chemosensing. In particular, for resistive gas sensing it is necessary that, due to the interaction with gas, a negative (or positive) charge is trapped at the surface, on the other hand this is not needed for catalysis. For instance, it can be thought that low temperature catalysis involves non-ionized adsorbed oxygen, chemisorbed but with a negligible charge transfer [40-43].

Figure 4 about here

As expected the presence of Pd is found to be extremely relevant for CO conversion, and the half-conversion temperatures, $T_{50\%}$, for Pd added materials, are ~70 °C lower than the one of the base material. It will be seen later if this means also an improved CO sensing for these materials. Also the understoichiometry of material B has a beneficial effect on CO conversion.

3.3. TPD and TPR experiments.

O_2 TPD and H_2 TPR provide useful information about the oxidability of the metal ions, the activity of the surface and bulk oxygen ions, and the stability of the material.
In particular, O_2 TPD allows to get information about oxygen adsorption at the surface. O_2 TPD profiles usually exhibit three oxygen desorption peaks: the first two located at low temperatures, due to adsorbed oxygen (α-type) and surface lattice oxygen (α'-type), and a third one placed at high temperatures associated to bulk lattice oxygen (β type). In particular, as far as α-oxygen is concerned, for similar materials, a desorption peak at T < 200 °C can be attributed to adsorbed ions O_2^- and desorption peaks at 300 °C ≤ T ≤ 500 °C to adsorbed ions O^-/ O^{2-}, whereas the desorption peak at 500 °C < T < 700 °C is attributed to surface lattice oxygen ions O^{2-} [44]
α-oxygen is expected on the $YMnO_3$ surface, like on any oxide. In fact in the presence of a surrounding atmosphere containing oxygen a continuous oxygen exchange is expected based mainly on adsorption/desorption with charge transfer (chemisorption) reactions [44-45]:

$$O_{2(gas)} + e^- \rightleftharpoons O_2^-{}_{(ads)} \quad (1a)$$
$$O_{2(gas)} + 2e^- \rightleftharpoons 2O^-{}_{(ads)} \quad (1b)$$
$$O_{2(gas)} + 4e^- \rightleftharpoons 2O^{2-}{}_{(ads)} \quad (1c)$$

The three reactions (1a-c) do not create lattice ions O^{2-} on the surface but surface charged species (α-oxygen) which can occupy surface oxygen vacancies, or adsorb at cations in higher

oxidation states [4][45-46]. These negatively charged types of oxygen are the so called suprafacial species because of their mobility and reactivity. Therefore, these chemisorbed oxygen species are sufficiently mobile to give a reactivity characterized by a low apparent activation energy.

The presence of peaks related to oxygen chemisorption can be very important since traditionally, in the literature, the low temperature chemoresistive behavior is fully explained by the presence of highly reactive surface chemisorbed O^- ions [23-24]. On the other hand, it was recently pointed out that in many cases the sensor response is partially or completely due to direct chemisorption of the target gas on the surface [26][47-50]. So the presence/absence of low temperature peaks may not be sufficient to describe the gas sensing properties of the material under study. In any case it is very important to use the TPD analysis to evaluate, for instance, the material stability.

Figure 5 about here

As shown in Fig. 5, in tested samples A and B no α'-oxygen peak is observed until 850 °C. The peak, if present, is therefore supposed to occur at higher temperature. Exceptions are materials containing Pd: for these samples α'-oxygen is desorbed at a temperature of about 700 °C. The presence of surface adsorbed oxygen species (possibly chemisorbed and reactive O^-/ O^{2-}) is enhanced in all the modified materials and the most relevant peak is that of defective material B. Other weakly adsorbed oxygen species, that probably participate to CO oxidation for Pd-added samples (see the results in the previous sub-section) could have been desorbed at low temperature during the pretreatment and cannot be excluded.

H_2 TPR analysis aims at determining the surface reducibility and can be related to chemoresistive response to reducing gases. Actually also in this context, for reasons analogous to those already presented concerning the O_2 TPD, it has to be stressed that the relationship between TPR results and chemoresistive sensitivity is not straightforward.

During H_2 TPR analysis, metal ions are reduced to ions with lower valences or metal atoms by H_2, and oxygen (chemisorbed, surface, bulk) may be concerned in the reduction reaction. Therefore, the reduction peaks reflect not only the oxidability of the metal ions but also the

activity of oxygen species, giving information similar to those obtained by CO conversion analysis and TPD.

Figure 6 about here

In Fig. 6 the results of TPR for some prepared powders are shown. The peaks related to the reaction with lattice oxygen are observed at a temperature in the interval 600 °C -700 °C, with the exception of the materials defective in Y: for this sample lattice oxygen seem to react at a temperature of about 450°C, close to the expected operating temperature range for chemoresistors. For this reason this material is the only one, among those tested, which is considered not suitable for stable operation as a conductive gas-sensors. In fact the involvement (consumption) of lattice surface/bulk oxygen in the reactions occurring during sensor operations can modify reversibly or irreversibly the surface/bulk composition and the electro-physical properties of the material, and can cause response drifts or instability.

Low temperature peaks are quite small for the other materials. It can be thought that weakly adsorbed oxygen species, that probably participate to CO oxidation for Pd-added samples (see the results in the previous sub-section) could have been desorbed at low temperature during the pretreatment. The oxygen participating in CO oxidation for the base material and for the defective powder B corresponds probably to the peak at about 280 °C for the defective and 340 °C for the stoichiometric in the H_2 TPR plot.
From these results it can be expected that Pd-added and defective materials will have the larger response to reducing gases, even if the enhancement of the activity due to pre-adsorbed oxygen with respect to the base material is quite small. Note that the chemoresistive response due to direct adsorption of the target gases cannot be predicted by means of this test.

4. Experimental results and discussion: gas sensing behavior

4.1. Theoretical background

In order to correlate the results shown in the previous sections with those reported in this section, concerning the behavior of the tested materials as gas resistive sensors, it is worth summarizing

some concepts. The most important consideration is that the behavior related to TPD, TPR, and especially catalytic activity towards CO are essentially surface processes, whereas, even if the resistive behavior in the studied temperature range depends mostly on similar surface reactions, the electrical response of the sensors always involves also the bulk electronic properties, and, above all, the resistive behavior depends only on the charge transfer between adsorbates and surface, so it is due only to those surface reactions involving also ionization or neutralization of ionized species. In this context the properties of the proposed material are discussed in the following.

As far as the electronic properties are concerned it must be remembered that the ionic bonds in the studied materials give to the atoms a very stable configuration: $2s^2 2p^6$ for O^{2-}, $4s^2 4p^6$ for Y^{3+} $3s^2 3p^6 3d^4$ for Mn^{3+}. The most important modification of the energetic levels which the atomic orbitals undergo in the crystal structure is the one regarding 3d orbitals of the Mn atom, because 3d orbitals are split and give rise to the top of the valence band and to the bottom of the conduction band [12] divided by a bang gap that was experimentally determined to be between 1.28 eV and 1.55 eV [51]. Lattice oxygen ions (O^{2-}) are filled and stable and therefore they have little importance for conduction unless, as well known, holes are present in the neighboring positions. As such the chemoresistive behavior is that of a medium band gap semiconductor, and, since it is observed that $YMnO_3$, as many ternary oxides, is a p-type semiconductor, it appears evident that acceptor levels are formed inside the band gap.

In the literature many works point out that $YMnO_3$ materials are characterized by the presence of a certain amount of Mn^{4+}, since Mn can be stable at a higher oxidation state than +3 while, according to [22], a distortion of the crystal structure accompanies understoichiometry of oxygen. On the other hand, the evident presence of acceptor extrinsic states rather indicates an overstoichiometry or oxygen or understoichiometry of metals at least in the bulk, as also required by electroneutrality [11]. In fact the formation of Mn^{4+} ions must create centers of positive charges, which can accept electrons (counterbalanced by interstitials oxygen ions). In any case, as it will be shown in this section, the δ values found for over/understoichiometry of oxygen in Sec III.A are in quite good agreement with the experimental data concerning the chemoresitivity (Fig. 7) if we take into account that the negative δ values are not sufficient to change the behavior of the material from a p-type to a n-type semiconductor.

The presence of oxygen vacancies found in [22] refers, from the experimental method used, to the surface, suggesting a large sensitivity to oxidizing gases. Indeed, the presence of anion vacancies on the surface provides a suitable driving force for adsorption of oxidizing gases. It also explains the similarity in reactivity and selectivity of material-derived oxygen and gas-phase originating oxygen for a given catalyst system. However, the type and valence of the neighboring cations, the M-O bond lengths, and the degree of covalence introduce the variations in reactivity observed for different complex metal-oxide systems.

As a final comment it can be noted that the evidence of Mn^{4+} on the surface found, e.g., in [6], can also be related to the following reaction in which the hole carrier can play a role.

$$Mn^{+3} + h^{+} \rightarrow Mn^{+4} \quad (surface) \qquad (2)$$

From reaction (2) it is expected that the sensing layer is formed by a p-type semiconductor, with a depleted surface and with a certain amount of trapped positive charge on the surface.

The SEM images in Fig. 2 show the complex morphology of the powder, each grain is a fine network of nano-crystallites, so the conductive behavior of the film is really not simple to derive [11][52-54]. Nevertheless, in order to have a reference for the following discussion, we will use the simple description of the sensor response as derived for a film consisting of loosely bound large grains. It is well known that when the sensing film is a set of large grains (with respect to the Debye length) with a small contact area, then the conduction in the film is described by percolation and mainly determined by the potential barriers at the grain boundaries [44][47-49]. The height of the barriers depends on the total amount of charge trapped at the surface, comprising the chemisorbed gas molecules. This model is based on the hypothesis that the electric field at the surface opposes the passage of free carriers from a grain to the neighbors. In the case of the tested samples of $YMnO_3$, which always show a p-type semiconductor behavior, this means that the net charge at the surface is positive, that could be justified by reaction (2): in detail, the presence of intrinsic ionized surface defects, such as Mn^{4+} creates, under the surface, a layer depleted of carriers (holes). From these assumptions the resistance can be written [55]:

$$R = R_A \exp\left(\frac{q^2 N_S^2}{2p_b \epsilon kT}\right) = R_A \exp\left(\frac{qV_S}{kT}\right) \qquad (3)$$

where R_A is a pre-exponential factor related to film geometry and to bulk properties of the material, weakly dependent on the temperature, k is the Boltzmann constant, T is the absolute

temperature, ε is the dielectric constant, p_b indicates the bulk density of carriers (holes), whereas N_s indicates the surface density of positively ionized states, and consequently, qN_s is the positive charge surface density. In the rightmost term $V_s = qN_s^2/2p_b\varepsilon$ is the potential barrier height at the grain boundary.

In particular N_s can be expressed as follows [43][47]:

$$N_s = N_i - [Z^-] + [X^+] \quad (4)$$

where N_i is the surface density of intrinsic positively ionized surface states, whereas $[X^+]$ and $[Z^-]$ indicate the surface densities of the positively and negatively ionized species X or Z, which are chemisorbed on the surface.

Note that if the adsorbed negative charge density is large due to an excess of adsorbed anions (large $[Z^-]$ term in Eq. (4)), the net charge on the surface becomes negative, and the conductions mechanism changes [50]: the surface carrier density is enhanced with respect to the bulk, the electrical filed at the grain boundary doesn't oppose the passage of carriers from a grain to the neighbor, and the resistance, mainly determined by the contribution of the grain bulk, cannot be expressed by Eq. (3).

The relationship in Eq. (3), although an approximation for the material under study, gives in any case an idea of the main dependencies and features of the sensor response, as shown in the literature [11][56], and it can be used as a base for the discussion of the experimental data and for the understanding of the sensing mechanism. With this model, the behavior is entirely explained by surface reactions.

In the tested conditions we expect to have negatively charged species from air oxygen, especially in the form of dissociated O^- that will decrease the N_s value and hence the sensor resistance, and OH^- and H^+ from the water vapor in humid environments, which usually produce, with reactions that are still under study, a net increase of the resistance [53]. Finally, in the presence of reducing gases, we expect an increase of N_s, due both to direct chemisorption (increase of $[X^+]$) and to the reaction with pre-adsorbed oxygen (decrease of $[Z^-]$), if present. On the other hand, in the presence of oxidizing gases we expect a decrease of the density of positively charge density on the surface due to direct chemisorption (increase of $[Z^-]$).

4.2. Resistance baseline analysis

In Fig. 7a the baseline resistance of the sensing film, R_0, is measured in steady state conditions for different temperatures in different chemical environments that are used as references. In particular dry and humid air are compared with dry and humid N_2 (inert gas). The comparison is summarized in Fig. 7b, where it can be seen that the difference of the baseline resistance in dry air and dry N_2 can be ascribed to a different density of surface charge ΔN_s, and, consequently to the difference of the barrier height, $\Delta V_s = \Delta(qN_s^2/(2p_b\varepsilon))$ which is plotted as a function of the temperature.

In Fig. 7b the value of ΔV_s, is evaluated by the following formula:

$$\Delta V_s = \frac{kT}{q} ln\left(\frac{R_{air}(T)}{R_{N_2}(T)}\right) \qquad (5)$$

where $R_{air}(T)$ and $R_{N2}(T)$ are measured at the same temperature, in dry air and in nitrogen.

There is a relationship between the resistance measurements and the O_2 TPD results of Fig. 5: actually the material with the evidence of a larger desorption of oxygen (material B - $YMn_{0,9}O_3$) is the one characterized by the maximum difference between the baseline resistance in air and in nitrogen, and hence with the maximum assessed ΔV_s that, comparing dry environments, could be totally attributed to $[O^-]$. Nevertheless the presence of adsorbed oxygen for this material is confined to the range of 'low temperatures' from 200 °C to 260 °C. The Pd-added material (material C), with large concentrations of dopant, seems instead to chemisorb oxygen only at higher temperatures (> 260 °C). Nevertheless, the value of the film resistance for this material is very high and at low temperature, measured resistance values are close to the full scale of the measurement system and a low accuracy is expected. The desorption peaks around 300 °C are correlated to a decrease of the adsorbed oxygen, so the ΔV_s decreases for all materials around this temperature. The Pd-added powder (material D) is characterized by a higher temperature of this first peak, that is perfectly consistent with the temperature at maximum ΔV_s.

From data in Fig. 7 it can be seen that the effect of water in N_2 is negligible for all materials, whereas in air there is an appreciable decrease of resistance for the stoichiometric material (material A) and even a larger one for $YMn_{0.9}O_3$ (material B).

Figure 7 about here

4.3. Response to gases

In this section the gas sensing properties will be assessed by means of both oxidizing and reducing gases, and will be correlated with the results of the previous analyses in order to gain an insight in the sensing mechanisms that can be considered also for other metal oxides.
The concentration range for each test gas is selected in accordance to the limits set by EU regulations for environmental monitoring.
The tests were performed using at least 3 sensors for each material. Each measurement cycle was repeated at least three times. The reproducibility of the results is satisfactory, characterized by differences lower than 20% among the individual devices. The short time stability (hours) is about 2%, whereas the medium time stability (days/months) of the baseline resistance value is close to 5%.
In the following subsections the response, Resp, of the sensor is reported in different conditions. Resp is defined as:

$$Resp = \frac{(R(t_{end}) - R_{0\infty})}{R_{0\infty}} \, x \, 100 \qquad (6)$$

where $R(t_{end})$ indicates the value assumed by the resistance at the end of exposure to the target gas, $R_{0\infty}$ is the steady state value of the film resistance in the carrier gas (air or nitrogen).
The results shown hereafter were usually obtained by testing the sensors at a fixed temperature in a constant flow of carrier gas for 8 minutes, than injecting a NO, NO_2 or CO mixture for 4 minutes, and then allowing the recovery in the carrier gas for 8 minutes before the next mixture injection.

4.3.1. Response to NO_2 and NO

The materials were tested with mixtures of air or nitrogen and NO_2. Representative results for five tested materials are shown in Fig. 8. In this figure the responses vs. time obtained with dry air as carriers gas and with a sequence of mixture pulses (23 ppm, 12 ppm and 6 ppm of NO_2, respectively) are shown for different sensor temperatures. The shape of the responses in nitrogen/NO_2 are clearly different for two groups: the first (material A and E) shows a similarly low response, while the second (materials B, C and D) shows a considerable response, especially

at lower temperatures. This suggests that the defect chemistry of the $YMnO_3$ material is more important, in NO_x sensing, than the presence of Pd.

Figure 8 about here

All materials show a response due to two different reactions: one is an oxidation of the surface whereas the other is a reduction. The two reactions are favored in two different ranges of temperature and are characterized by different dynamics, in particular the oxidizing reaction is favored at lower temperatures and is much faster than the reduction. In air mixtures this can be easily explained adopting the reaction paths proposed for many other materials (for metal oxides used both as catalysts and as sensors). In particular the following oxidation reaction can be assumed [55][57-59]:

$$(NO_2)_{gas} + S_{NO_2} \leftrightarrow NO_2{}^{-}{}_{ads} + h^{+} \qquad \text{low T}, \qquad (7)$$

where S_{NO2} represents an adsorption site for NO_2, and $NO_2{}^{-}{}_{ads}$ a chemisorbed molecule bound to the adsorption site. Reaction (7) shows how a negative charge gets trapped on the surface and a hole is released: both these effects contribute to a resistance decrease.

A possible route for reduction of the surface is [55][57-59]:

$$(NO_2)_{gas} + O^{-}{}_{ads} + h^{+} \leftrightarrow (NO)_{gas} + (O_2)_{gas} + S_O \qquad \text{high T} \qquad (8)$$

Here $O^{-}{}_{ads}$ indicates negatively ionized oxygen on the surface.
Reaction (8) shows that a negative charge trapped on the surface is freed, accompanied by the loss of a hole: both the mechanisms contribute to the increase of the resistance.
In Fig. 9 the response of the tested materials in nitrogen, air, humid air, or humid nitrogen and 10 ppm NO_2 is shown as a function of the film temperature.

Figure 9 about here

It can be seen that the reduction of the surface is relevant especially for the stoichiometric material A, which essentially responds to NO_2 at temperatures higher than 250 °C with an increase of the value of the resistance. The oxidation of the surface is more pronounced for the

defective material B that is characterized by a large response at temperatures of about 180 °C (-30% @ 10 ppm).

Fig. 10 shows the responses to NO_2 (air or N_2 as carrier gas, dry and humid conditions) as a function of gas concentration at the optimum temperature for material B (180 °C) and C (200 °C). It is evident, also in this range of concentrations, that the responses of these sensors are, as expected (see Eq. (3)), strongly non linear.

Figure 10 about here

It is worth noting that in reaction (8) ionized atomic oxygen plays a role. In air mixtures chemisorbed oxygen is the species involved, but in nitrogen no chemisorbed oxygen is expected. Hence the response in nitrogen should not involve any surface reduction. Moreover, from TPR and TPD results, the largest quantity of reactive oxygen has been observed for the defective material B, nevertheless, as shown by Fig. 9, this material shows a small positive increase of resistance at high temperature. From these observations it appears that also a different reaction has to be accounted for.

A possible route is the following: NO_2 dissociation can be followed by NO chemisorption, so that reaction (8) can be replaced by [60]:

$$\begin{aligned} &(NO_2)_{gas} + (S_{NO}) + h^+ \leftrightarrow NO_{ads}{}^+ + 1/2(O_2)_{gas} \\ &NO_{ads}{}^+ \rightarrow (NO)_{gas} + h^+ \qquad \text{high T} \end{aligned} \tag{9}$$

Exploiting the reactions (7) and (9) a model for the sensing mechanism in nitrogen is presented in the following.

As an approximation of the kinetics of the sensor response, a first order reaction can be used to describe reactions (7) and (9). In this case the two following differential equations can be used to describe the oxidation reaction (7) and the reduction reaction (9) of the surface in nitrogen:

$$\frac{d([NO_2^-{}_{ads}])}{dt} = k_1 \left[NO_{2_{gas}}\right] \left([S_{NO_2}] - [NO_2^-{}_{ads}]\right) - k_{-1}[NO_2^-{}_{ads}][h]^+ \tag{10}$$

$$\frac{d([NO^+_{ads}])}{dt} = k_2[h^+] \left[NO_{2_{gas}}\right] ([S_{NO}] - [NO^+_{ads}]) - k_{-2}[NO^+_{ads}], \tag{11}$$

where k_i, i=(1,-1,2,-2), are the reaction rate constants of reactions (7) and (9), respectively, depending on temperature, $[NO_{2_{ads}}^{-}]$ is the density of the chemisorbed NO_2, whereas $[NO_{ads}^{+}]$ is the density of chemisorbed NO. $[NO_2^-]$ and $[NO^+]$ have to be considered as contributions to the negative and positive charge trapped at the surface and have to be included in the terms $[Z^-]$ and $[X^+]$ of Eq. (4) so that:

$$N_s = N_i - \left[NO_{2\ ads}^{-}\right] + [NO_{ads}^{+}] \tag{12}$$

If the carrier gas is dry air, Eq. (10) has to be modified including also the kinetics of oxygen chemisorption from air.

Even the simple model shown in Eqs. (10) and (11) is non linear because $[h^+]$ on the surface is related exponentially to the height of the surface barrier; in fact, usually, the density of surface carriers can be written as follows [11][43][47][61] :

$$[h^+] = p_b \exp\left(-\frac{qV_s}{kT}\right) = p_b \exp\left(-\frac{q^2 N_S^2}{2\,\epsilon kT p_b}\right) \quad , \tag{13}$$

where V_s is the voltage barrier height.

Note that the exponential function in Eq. (13) is exactly the reciprocal of the exponential function appearing in the expression of the resistance in Eq. (3). It can be seen that in the experimental conditions used in this work (see Figs. 8 and 9) the relative variations expected for this function are lower than 0.5, so a constant value can be used to approximate the hole density. In this way at constant temperature Eqs. (10) and (11) become linear differential equations with constant coefficients. Therefore a very simple approximation for the sensor behavior can be found. In this case the coefficients of the two differential equations are constant and the transient behavior of N_s during gas exposure (gas injection at t=0) can be written as follows:

$$N_s(t) = N_i - A_{ox}\left(1 - \exp\left(-\frac{t}{\tau_{ox}}\right)\right) - \left[NO_{2\ ads}^{-}\right](0^-)\exp\left(-\frac{t}{\tau_{ox}}\right) +$$

$$+A_{red}\left(1 - \exp\left(-\frac{t}{\tau_{red}}\right)\right) + [NO^{+}{}_{ads}](0^-)\exp\left(-\frac{t}{\tau_{red}}\right) \tag{14}$$

where:

$$A_{ox} = \left[NO_{2\ ads}^{-}\right]_{\infty} = \frac{k_1\left[NO_{2_{gas}}\right]\left[S_{NO_2}\right]}{k_{-1}[h^+] + k_1\left[NO_{2_{gas}}\right]};$$

$$A_{red} = [NO^+{}_{ads}]_\infty = \frac{k_2\left[NO_{2\,gas}\right][S_{NO}][h^+]}{k_{-2} + k_2\left[NO_{2\,gas}\right][h^+]}$$

$\tau_{ox} = \frac{1}{k_1\left[NO_{2\,gas}\right]+k_{-1}[h^+]}$; $\tau_{red} = \frac{1}{k_{-2}+k_2[NO_{2\,gas}][h^+]}$.

Note that, according to the proposed model, a large density of holes reduces the sensitivity of the sensors to surface oxidation but not to surface reduction. Both reactions are faster the larger is the concentration of the surface holes. This explains the experimental response: Pd-added materials show a large resistance, an enhanced oxidation and a smaller reduction with respect to the stoichiometric material. Moreover, it can be seen how the response to larger concentrations of gas becomes faster.

During the recovery phase the N_s time-evolution can be written in the following manner:

$$N_s(t) = \mathrm{N_i} - \left[NO_2^-{}_{ads}\right](t_{start}) \exp\left(-\frac{t-t_{start}}{\tau^r_{ox}}\right) + [NO^+{}_{ads}](t_{start}) \exp\left(-\frac{t-t_{start}}{\tau^r_{red}}\right). \quad (15)$$

In Eq. (15) $t > t_{start}$ (recovery phase starting at t_{start}), and τ^r_{ox} and τ^r_{red} are evaluated as in Eq. (14) but with $[NO_2]$ equal to 0.

The results obtained fitting the experimental data with nitrogen as carrier gas, at different temperatures, are reported in Fig. 11. The fitted sensor responses are shown together with experimental data for two different materials (A ($YMnO_3$) and D ($YMn_{0.95}Pd_{0.05}O_3$)) when three pulses of NO_2 mixtures are injected with concentrations 23 ppm, 10 ppm and 6 ppm, respectively. Different colors correspond to different temperatures in the range 180 °C - 240 °C (fitting error about 10%). The most relevant parameters estimated in the first gas injection phase are shown in Fig. 12 and Table III. The parameter estimation procedure and the model fitting are described with more details in Appendix A.

It can be seen that surface oxidation is the fastest process (one order of magnitude faster), and is the most relevant reaction at lower temperatures. The introduction of Pd and of defects has a strong influence on both the reduction and the oxidation processes, and in particular all of them have a larger oxidation response, whereas reduction almost disappears only for material C ($YMn_{0.9}Pd_{0.1}O_3$).

Even if the Pd-free defective material B responds faster and has a larger response at lower temperatures (optimum temperature 180 °C) with respect to the Pd-added defective material C, this latter has to be considered as the best performing material since it can be seen (see Fig. 8 and Fig. 9) that, while having a large response to the target gas (20% @6 ppm), it is less sensitive to temperature changes and to the presence of humidity for temperatures larger than 220 °C.

Figure 11 about here

Figure 12 about here

The materials were tested using the same measurement protocol also with NO mixtures (air and nitrogen as carrier gases). All materials have a very limited sensitivity toward this gas. In nitrogen and in air both oxidation and reduction of the sensor surface is possible at different temperatures: oxidation is favored at low temperatures whereas reduction occurs at higher temperatures. $YMn_{0.9}Pd_{0.1}O_3$ (material C) and the stoichiometric material (material A) have the largest responses; the stoichiometric material is mainly reduced (15% @23 ppm NO, 260 °C), whereas the defective material B is oxidized (10% @23 ppm, 180 °C) as it can be seen in Fig. 13.

Figure 13 about here

4.3.2. Response to CO

Figure 14 about here

Figure 15 about here

The response to CO of the base material is limited, and, as it can be seen from figure 14 for material E, responses are fast enough only at temperatures larger than 300 °C. The addition of Pd in $YMn_{1-x}Pd_xO_3$ materials (materials C and D) does not favor the reduction of the surface, in fact

it can be seen, comparing the responses of these materials with those of the stoichiometric material (material A), that the sensitivity is lowered. Better results are found, instead, with the defective material B, but the response is still limited. An effective improvement is reached by impregnation of the surface with Pd (material E): at 300 °C the response to 1000 ppm CO in air is 80%.

The responses to CO (dry air or N_2 as carrier gas) are reported in Fig. 15 as a function of CO concentration. The responses of the three best performing materials at the optimum temperatures (materials A @ T=320 °C, B @ T=320 °C and E @300 °C) are compared. The response to CO, in this CO concentration range, is close to a linear behavior, in contrast with the response to NO_2 shown in Fig. 13.

The results found for CO confirm the previous discussion. In particular, by comparing the responses in nitrogen with those in air, it can be seen that all the materials respond better in the inert carrier gas. Moreover, it can be seen that the enhancement in CO conversion at low temperature is not reflected at all in an improvement of the resistive sensing [62].

In order to understand these observations, it must be remembered that the response to CO of metal oxide resistive sensors is explained by two possible reactions:

$$(CO)_{gas} + S_{CO} + h^+ \leftrightarrow CO^+_{ads} \quad (16)$$

$$(CO)_{gas} + O^-_{ads} + h^+ \rightarrow (CO_2)_{gas} \quad (17)$$

The first one is a reversible chemisorption [47-49], which consumes (presumably) a hole by donating an electron: the resistance grows since N_s increases due to the formation of $[CO^+_{ads}]$ (compare with Eqs. (3) and (4)).

The second one, which is the most used by the researchers to model the chemoresistive behavior (see, e. g., [23-24]), is an irreversible oxidation of CO that consumes a pre-adsorbed oxygen releasing the electron trapped by this latter (consuming probably a hole): the resistance grows due to an increase of N_s related to a decrease of the density of surface negative charged species (see Eqs. (3) and (4)), as well as a decrease of the hole density.

The analysis of the experimental data concerning CO sensing reported in this sub-section suggests the following hypotheses:

1) The response of many oxide chemoresistors and in particular of all the tested materials is mainly due to the direct chemisorption of CO on the surface of the sensing layer, according to reaction (16). This hypothesis is supported by the comparison of the measurement in air (presence of oxygen) and in nitrogen where no (or a little quantity of chemisorbed oxygen) is present. The response to CO is larger in nitrogen.
2) The oxygen species involved in CO conversion are not those determining the resistive response. This hypothesis is suggested by the comparison of the results of CO conversion tests with resistance measurements.
3) The presence of chemisorbed oxygen, which makes reaction (17) a possible route of CO oxidation and can contribute to the resistive response magnitude, doesn't boost the response. On the contrary, the presence of adsorbed oxygen might decrease the CO response by reducing the value of N_s, changing the working point of the sensor and consequently its sensitivity. In fact from Eq. (3) we find:

$$\frac{dR}{dN_s}\frac{1}{R} = \frac{q^2 N_s^2}{\epsilon k T p_b} \tag{18}$$

5. Conclusions

In this work the preparation and characterization of chemoresistive sensors for NO_x and CO based on hexagonal $YMnO_3$ are presented: the tested sensors are based on the stoichiometric material, on non-stoichiometric materials and on materials added with palladium.

For $YMnO_3$, as for many transition metal ternary oxides, the chemistry of the defects is shown to be fundamental to determine the gas sensing properties in terms of shape, speed and magnitude of the response, and can be used to tailor the sensor selectivity. Oxygen defects seem to enhance the response to oxidizing gases and to NO_2 in particular. In fact it can be seen from the results presented in the paper that the stoichiometric material (material A) has a low response to NO_2 (less than 3% percent @ 10 ppm 200 °C) whereas the response of the most defective material (material B) is more than ten times larger (-30% @ 10 ppm and 180 °C). The optimum

temperature of material B is the lowest of all tested materials. The response to NO_2 of this and the other tested material can be explained by a simple model which involves direct adsorption on the surface and two different reactions, one that creates extrinsic acceptor states, favored at low temperature, and the other, favored at high temperature, that creates donor states.

Also the addition of Pd leads to an improvement in terms of response to NO_2 and the best results are obtained with $YMn_{0.95}Pd_{0.05}O_3$ (material D). The Pd added materials show a smaller sensitivity of the resistance to the temperature that makes them more robust for gas sensing applications.

Regarding CO, the Pd impregnated material has a clearly higher response suggesting that only metallic Pd on the surface might be useful for the formulation of a CO sensor based on $YMnO_3$.

Moreover the stoichiometric material A responds to CO more than the other modified materials (with the only exception E). Therefore, even if Pd on the surface effectively enhance the CO response, the modified stoichiometry which was found for material C and D is eventually more influent and decreases the response to CO.

Generally speaking, there is no relationship between the oxygens involved in catalysis and those involved in sensing. The working temperatures are in any case very different. Moreover, the presence of oxygen seems not necessary for sensing, and can be even counterproductive, for example by inducing smaller values of N_s, which reduces the sensitivity.

All the materials proved to be satisfactorily stable. The sensitivity to humidity is limited. On the other hand there are problems of sensitivity to the temperature: only the Pd containing materials C and D can be easily used as sensors; the other materials require a very accurate temperature control.

Acknowledgements

Thanks are due to Andrea Scala, Conservation of Cultural Heritage Research Unit, DSFTA, University of Siena, for providing us with the X-ray powder diffraction data.

Appendix A

The model described by Eqs. (10)-(15) is fitted to the experimental data using a non-linear fitting method.

To reduce to a minimum the number of parameters to be estimated and to get a robust model, Eqs. (10)-(15) are rewritten for the normalized value of N_s, i.e. $N_s' = qN_s/\sqrt{2\epsilon k p_b}$. To this aim, indicating with x' the quantity x multiplied by $\alpha = q/\sqrt{2\epsilon k p_b}$ (i.e. $x' = \alpha x$) we can write:

$$N_s'(t) = N_i' - A_{ox}'\left(1 - \exp\left(-\frac{t}{\tau_{ox}}\right)\right) - \left[NO_2^-{}_{ads}\right]'(0^-)\exp\left(-\frac{t}{\tau_{ox}}\right) +$$

$$+A'_{red}\left(1 - \exp\left(-\frac{t}{\tau_{red}}\right)\right) + \left[NO^+{}_{ads}\right]'(0^-)\exp\left(-\frac{t}{\tau_{red}}\right) \qquad \text{(A.1)}$$

Eq.(15) can be rewritten in the same way:

Moreover we have, from Eq. (3):

$$R(t) = R_A \exp\left(\frac{N_s'(t)^2}{T}\right) \qquad \text{(A.2)}$$

The normalized parameters appearing in Eq. (A.1) and (A.2), R_A, A_{ox}', A_{red}', τ_{ox}, τ_{red}, and τ^r_{ox}, τ^r_{red} depend on many physical/chemical quantities that do not need to be individually assessed in order to model the behavior of the resistance. The parameters in Eqs. (A.1) and (A.2) were estimated by using LSQNONLIN Matlab function.

The fitting procedure starts using initial values of all the parameters R_A, $\left[NO_2^-{}_{ads}\right]'(0^-)$, $\left[NO^+{}_{ads}\right]'(0^-)$, A_{ox}', A_{red}', τ_{ox}, τ_{red}, and τ^r_{ox}, τ^r_{red}, to compute $N_s'(t)$ and $R(t)$ from the Eqs. (A.1) and (A.2). After this, the mean square error between the model output and the measured resistance $R(t)$ is evaluated. The parameters are varied automatically searching for the minimum error until a stop criterion is met.

Finally, note that A_{ox}', A_{red}', τ_{ox}, τ_{red}, and τ^r_{ox}, τ^r_{red} depend both on temperature and on gas concentration, so a different set of parameters is needed for each temperature and for each NO_2 concentration. Therefore they are estimated for each NO_2 concentration, using measurements performed at constant temperature during chemical transients.

Note that the value of R_A can be considered constant for each single sensor. In fact, in the expression of resistance of eq. (3), $R_A \sim (\gamma p_b\, q\, \mu_b)^{-1}$ has a weak dependence on temperature with respect to the strong exponential dependence and is usually considered constant. This is true if all the bulk acceptors are ionized.

A more robust model can be obtained by reducing the number of the parameters to be estimated, using for R_A a value assessed by an experimental method. In particular the R_A estimate is obtained by inducing a very fast thermal transient from T_1 to T_2 (at $t=t_0$) and letting the chemical environment unchanged. In this way at the beginning of the transient the value of N_s can be considered constant, with $N_s(t_0^-) = N_s(t_0^- + \Delta t)$ if $\Delta t << t_{resp}$, where t_{resp} is the chemical response time at the higher temperature, and $\Delta t >> t_{thermal}$, where $t_{thermal}$ is the thermal rise time of the system. This procedure is possible if the temperature is controlled by a closed loop system, which enables reducing thermal transients duration (in our case the thermal time constant is about 1 s and $t_{thermal} \approx 5$ s). In this case the value of R_A can be assessed from the following equations:

$$R_2 = R(t_0 + \Delta t) = R_A \exp\left(\frac{q^2 N_s^2(t_0^-)}{2kT_2 \epsilon p_b}\right) \quad (A.3)$$

$$R_1 = R(t_0^-) = R_A \exp\left(\frac{q^2 N_s^2(t_0^-)}{2kT_1 \epsilon p_b}\right) \quad (A.4)$$

Hence:

$$\ln(R_A) = \frac{T_1 \ln(R_1) - T_2 \ln(R_2)}{T_1 - T_2} \quad (A.5)$$

References

[1] I. D. Kim, A. Rothschild, H. L. Tuller, Advances and new directions in gas-sensing devices. Acta Mater., *61*(3) (2013) 974-1000.

[2] G. Eranna , B. C. Joshi , D. P. Runthala, R. P. Gupta, Oxide Materials for Development of Integrated Gas Sensors—A Comprehensive Review, Crit. Rev. Solid State Mater. Sci., 29(3-4) (2004) 111-188.

[3] M. M. Natile, A. Ponzoni, I. Concina, A. Glisenti, Chemical Tuning versus Microstructure Features in Solid-State Gas Sensors: $LaFe_{1-x}Ga_xO_3$, a Case Study, Chem. Mater., 26(4) (2014) 1505-1513.

[4] Q. H. Zhang, X. Shen, Y. Yao, Y. G. Wang, C. Q. Jin, R. C. Yu, Oxygen vacancy ordering and its mobility in $YMnO_3$, J. Alloys Compd., 648 (2015) 253-257.

[5] G. Korotcenkov, Metal oxides for solid-state gas sensors: What determines our choice?, Mater. Sci. Eng. B, 139(1) (2007) 1-23.

[6] J. W. Fergus, Materials for high temperature electrochemical NO_x gas sensors, Sens. Actuators B, 121(2) (2007) 652-663.

[7] J. W. Fergus, Perovskite oxides for semiconductor-based gas sensors, Sens. Actuators B, 123(2) (2007) 1169-1179.

[8] M. Mori, Y. Itagaki, Y. Sadaoka, Effect of VOC on ozone detection using semiconducting sensor with $SmFe_{1-x}Co_xO_3$ perovskite-type oxides, Sens. Actuators B, 163(1) (2012) 44-50.

[9] S. Thirumalairajan, K. Girija, V. R. Mastelaro, N. Ponpandian, Surface morphology-dependent room-temperature $LaFeO_3$ nanostructure thin films as selective NO_2 gas sensor prepared by radio frequency magnetron sputtering, ACS Appl. Mater. Interfaces, 6(16) (2014) 13917-13927.

[10] H. T. Giang, H. T. Duy, P. Q. Ngan, G. H. Thai, N. N. Toan, Hydrocarbon gas sensing of nano-crystalline perovskite oxides $LnFeO_3$ (*Ln*= La, Nd and Sm), Sens. Actuators B, 158(1) (2011) 246-251.

[11] T. Addabbo, F. Bertocci, A. Fort, M. Gregorkiewitz, M. Mugnaini, R. Spinicci, V. Vignoli, Gas sensing properties and modeling of $YCoO_3$ based perovskite materials, Sens. Actuators B, 221 (2015) 1137-1155.

[12] W. Sotero, A. F. Lima, M. V. Lalic, Analysis of the Mn–O and Y–O bonds in paraelectric and ferroelectric phase of magnetoelectric $YMnO_3$ from the first principles calculations, J. Alloys Compd., 649 (2015) 285-290.

[13] A. Munoz, J. A. Alonso, M. J. Martínez-Lope, M. T. Casais, M. T. Fernández-Díaz, Magnetic structure of hexagonal $RMnO_3$ (R = Y, Sc): A Neutron Diffraction Study, Inorg. Chem., 39 (2000) 917-923.

[14] H. W. Brinks, H. Fjellvåg, A. Kjekshus, Synthesis of Metastable Perovskite-type $YMnO_3$ and $HoMnO_3$, J Solid State Chem., 129 (1997) 334-340.

[15] J. A. Alonso, M. J. Martínez-Lope, M. T. Casais, M. T. Fernández-Díaz, Evolution of the Jahn-Teller Distortion of MnO_6 Octahedra in $RMnO_3$ Perovskites (R = Pr, Nd, Dy, Tb, Ho, Er, Y): A Neutron Diffraction Study, Inorg. Chem., 39 (2000) 917-923.

[16] K. Bergum, H. Okamoto, H. Fjellvåg, T. Grande, M.-A. Einarsrud, S. M. Selbach, Synthesis, structure and magnetic properties of nanocrystalline $YMnO_3$, Dalton Trans., 40(29) (2011) 7583-7589.

[17] Z. Branković, G. Branković, M. Počuča-Nešić, Z. Marinković Stanojević, M. Žunić, D. Luković Golić, R. Tararam, M. Cilense, M.A. Zaghete, Z. Jagličić, M. Jagodič, J.A. Varela, Hydrothermally assisted synthesis of $YMnO_3$, Ceram. Int., 41(10) (2015) 14293-14298.

[18] J. E. Medvedeva, V. I. Anisimov, M. A. Korotin, O. N. Mryasov, A. J. Freeman, The effect of Coulomb correlation and magnetic ordering on the electronic structure of two hexagonal phases of ferroelectromagnetic $YMnO_3$, Journal of Physics: Condensed Matter, 12(23) (2000) 4947-4958.

[19] Landolt-Börnstein, Group III.16a, Ferroelectrics and Related Substances, K.H. Hellwege, M. Hellwege (Eds.), Springer, Berlin, 1981.

[20] A. J. Overton, J. L. Best, I. Saratovsky, M. A. Hayward, Influence of Topotactic Reduction on the Structure and Magnetism of the Multiferroic $YMnO_3$, Chem. Mater., 21 (2009) 4940–4948.

[21] S. Remsen, B. Dabrowski, Synthesis and Oxygen Storage Capacities of Hexagonal $Dy_{1-x}Y_xMnO_{3+\delta}$, Chem. Mater., 23 (2011) 3818–3827.

[22] A. G. Kochur, A. T. Kozakov, K. A. Googlev, A. V. Nikolskii, X-ray photoelectron study of temperature effect on the valence state of Mn in single crystal $YMnO_3$, J. Electron. Spectrosc. Relat. Phenom., 195 (2014) 1-7.

[23] D. R. Jones, T. G. G. Maffeïs, Analysis of the kinetics of surface reactions on a zinc oxide nanosheet-based carbon monoxide sensor using an Eley-Rideal model, Sens. Actuators B, 218 (2015) 16-24.

[24] A. Varpula, S. Novikov, A. Haarahiltunen, P. Kuivalainen, Transient characterization techniques for resistive metal-oxide gas sensors, Sens. Actuators B, 159 (2011) 12-26.

[25] K. Mukherjee, S. B. Majumderz, Analyses of Conductance Transients to Address the Selectivity Issue of Zinc Ferrite Gas Sensors, Electrochem. Solid-State Lett., 13(4), (2010) J25-J27.

[26] A. Fort, M. Mugnaini, S. Rocchi, V. Vignoli, Surface state models for conductance response of metal oxide gas sensors during thermal transients, in: G. Korotcenkov (Ed.), Chemical Sensors: Simulation and Modeling, Vol. 2: Conductometric-Type Sensors. Momentum Press, LLC, New York, 2012, pp.127-175.

[27] A. C. Larson, R. B. Von Dreele, General structure analysis system (GSAS), Los Alamos National Laboratory Report, LAUR 86-748 (2000).

[28] B. B. van Aken, A. Meetsma, T. T. M. Palstra, Hexagonal $YMnO_3$, Acta Cryst., C57 (2001) 230-232.

[29] G. Baldinozzi, J.-F. Bérar, G. Calvarin-Amiri, Rietveld refinement of two phase Zr-doped Y_2O_3, Mater. Sci. Forum, 278 (1998) 680-685.

[30] D. Okuyama, S. Ishiwata, Y. Takahashi, K. Yamauchi, S. Picozzi, K. Sugimoto, H. Sakai, M. Takata, R. Shimano, Y. Taguchi, T. Arima, Y. Tokura, Magnetically-Driven Ferroelectric Atomic Displacements in perovskite like $YMnO_3$, http://arxiv.org/abs/1107.2467v1.

[31] J. Waser, H. A. Levy, S. W. Peterson, The structure of PdO, Acta Cryst., 6 (1953) 661-663.

[32] R. W. G. Wyckoff, Cubic Closest Packed ccp Structure, Crystal Structures, 1 (1963) 7-83.

[33] T. Addabbo, F. Bertocci, A. Fort, M. Mugnaini, V. Vignoli, L. Shahin, S. Rocchi, Versatile measurement system for the characterization of gas sensing materials, in Proceedings of the 2013 IEEE International Instrumentation and Measurement Technology Conference (I2MTC), 2013 976-980 (doi: 10.1109/I2MTC.2013.6555561).

[34] A. Šutka, K. A. Gross, Spinel ferrite oxide semiconductor gas sensors, Sens. Actuators B, 222 (2016) 95-105.

[35] V. M. Goldschmidt, Geochemische Verteilungsgesetze der Elemente. VII. Die Gesetze der Krystallchemie. Skrifter Norske vidensk. Akad. Oslo, I: Mat. Natur., 2 (1926) 117-124.

[36] M. F. Zhang, J.-M. Liu, Z. G. Liu, Microstructural characterization of nanosized $YMnO_3$ powders: the size effect, Appl. Phys. A, 79 (2004) 1753-1756.

[37] A. Moure, T. Hungría, A. Castro, J. Galy, O. Peña, J. Tartaj, C. Moure, Doping influence on the stability of $YMnO_3$ orthorhombic perovskite obtained by mechanosynthesis, Mater. Chem. Phys., 133 (2012) 764-771.

[38] S. Ishiwata, Y. Tokunaga, Y. Taguchi, Y. Tokura, High-Pressure Hydrothermal Crystal Growth and Multiferroic Properties of a Perovskite $YMnO_3$, J. Am. Chem. Soc., 133 (2011) 13818-13820.

[39] D. W. Baker, P. A. Thomas, N. Zhang, A. M. Glazer, Structural study of $K_xNa_{1-x}NbO_3$ (KNN) for compositions in the range x = 0.24-0.36, Acta Cryst. B, 65 (2009) 22-28.

[40] J. L. G. Fierro (Ed.), Metal oxides: chemistry and applications, CRC Press, Boca Raton (FL), 2005.

[41] H. H. Kung, Oxygen on Oxides, in: Transition metal oxides: surface chemistry and catalysis, Vol. 45, Elsevier, Amsterdam, 1989, pp. 110-120.

[42] V. E. Henrich, P. A. Cox, The surface science of metal oxides, Cambridge University Press, Cambridge, 1996.

[43] J. Ding, T. J. McAvoy, R. E. Cavicchi, S. Semancik, Surface state trapping models for SnO_2-based microhotplate sensors, Sens. Actuators B, 77(3) (2001) 597-613.

[44] N. Barsan, U. Weimar, Conduction Model of Metal Oxide Gas Sensors, J. Electroceram., 7 (2001) 143-167.

[45] B. Levasseur S. Kaliaguine, Effect of the rare earth in the perovskite-type mixed oxides $AMnO_3$ (A= Y, La, Pr, Sm, Dy) as catalysts in methanol oxidation, J. Solid State Chem., *181*(11) (2008) 2953-2963.

[46] M. James, T. Tedesco, D. J. Cassidy, R. L. Withers, Oxygen vacancy ordering in strontium doped rare earth cobaltate perovskites $Ln_{1-x}\ Sr_x\ CoO_{3-\delta}$ (Ln= La, Pr and Nd; x> 0.60), Mater. Res. Bull., 40(6) (2005) 990-1000.

[47] A. Fort, M. Mugnaini, S. Rocchi, M. B. Serrano-Santos, V. Vignoli, R. Spinicci, Simplified models for SnO_2 sensors during chemical and thermal transients in mixtures of inert, oxidizing and reducing gases, Sens. Actuators B, 124(1) (2007) 245-259.

[48] M. Hübner, R. Pavelko, J. Kemmler, N. Barsan, U. Weimar, Influence of Material Properties on Hydrogen Sensing for SnO_2 Nanomaterials, Procedia Chem., 1 (2009) 1423–1426.

[49] M. Hübner, R.G. Pavelko, N. Barsan, U. Weimar, "Influence of oxygen backgrounds on hydrogen sensing with SnO_2 nanomaterials", Sens. Actuators B, 154 (2011) 264–269.

[50] N. Barsan, J. Rebholz, U. Weimar, Conduction mechanism switch for SnO_2 based sensors during operation in application relevant conditions; implications for modeling of sensing, Sens. Actuators B, 207 (2015) 455-459.

[51] C. Degenhardt, M. Fiebig, D. Fröhlich, T. Lottermoser, R. V. Pisarev, Nonlinear optical spectroscopy of electronic transitions in hexagonal manganites, Appl. Phys. B, 73(2) (2001) 139-144.

[52] A. Fort, M. Mugnaini, S. Rocchi, V. Vignoli, E. Comini, G. Faglia, A. Ponzoni, Metal-oxide nanowire sensors for CO detection: Characterization and modeling, Sens. Actuators B, 148(1) (2010) 283-291.

[53] A. Fort, M. Mugnaini, I. Pasquini, S. Rocchi, V. Vignoli, Modeling of the Influence of H_2O on Metal Oxide Sensor Responses to CO, Sens. Actuators B, 159(1) (2011) 82-91.

[54] A. Burresi, A. Fort, S. Rocchi, M. B. Serrano Santos, N. Ulivieri, V. Vignoli, Temperature profile investigation of SnO_2 sensors for CO detection enhancement, IEEE Trans. Instrum. Meas., 54(1) (2005) 79–86.

[55] A. Fort, T. Addabbo, V. Vignoli, F. Bertocci, M. Mugnaini, A. Atrei, M. Gregorkiewitz, Gas-sensing properties and modeling of silver doped potassium hollandite, Sens. Actuators B, 194 (2014) 427–439.

[56] T. Addabbo, F. Bertocci, A. Fort, M. Mugnaini, V. Vignoli, WO_3 nanograined chemosensor: a model of the sensing behavior, in press on the IEEE Trans. Nanotechnol., (doi:10.1109/TNANO.2016.2558099).

[57] P. L. Martin, A. P. Quoc, R. S. Glass, Effect of Cr_2O_3 electrode morphology on the nitric oxide response of a stabilized zirconia sensor, Sens. Actuators B, 96(1) (2003) 53–60.

[58] A. Afzal, N. Cioffi, L. Sabbatini, L. Torsi, NO_x sensors based on semiconducting metal oxide nanostructures: progress and perspectives, Sens. Actuators B, 171 (2012) 25–42.

[59] K. Wetchakun, T. Samerjai, N. Tamaekong, C. Liewhiran, C. Siriwong, V. Kruefu, A. Wisitsoraat, A. Tuantranont, S. Phanichphant, Semiconducting metal oxides as sensors for environmentally hazardous gases, Sens. Actuators B, 160(1) (2011) 580–591.

[60] G. R. Bamwenda, A. Obuchi, A. Ogata, J. Oi, S. Kushiyama, K. Mizuno, The role of the metal during NO_2 reduction by C_3H_6 over alumina and silica-supported catalysts, J. Mol. Catal. A: Chem., 126(2) (1997) 151-159.

[61] A. Fort, S. Rocchi, M. B. Serrano-Santos, R. Spinicci, V. Vignoli, Surface State Model for Conductance Responses During Thermal-Modulation of SnO_2-Based Thick Film Sensors: Part I—Model Derivation, IEEE Trans. Instrum. Meas., 55(6) (2006) 2102 – 2106.

[62] I. Kocemba, J. Rynkowski, The influence of catalytic activity on the response of Pt/SnO_2 gas sensors to carbon monoxide and hydrogen. Sens. Actuators B, 155(2) (2011) 659-666.

Tommaso Addabbo received the Ph.D. degree in information engineering from the University of Siena, Italy, where he is currently working as an research associate. His main research interests include analysis of nonlinear circuits and systems, stochastic aspects of chaotic dynamics, and analog circuits design. During his research program, he was a Visiting Scholar at the Institute of Nonlinear Science at the University of California, San Diego, and at the Macedonian Academy of Sciences and Arts in Skopje, Macedonia.

Francesco Bertocci was born in Pescia, Italy, on February 18, 1980. He received the M.S. degree in Eletronic Engineering in 2007 and the Ph.D. degree in Industrial and Reliability Engineering in 2011 from the University of Florence, Italy. His current research interests are design and development of different chemical sensors and their characterization through electrical and electronic instrumentation and measurements.

Ada Fort received the laurea degree in electronic engineering, in 1989 and the Ph.D. Degree in nondestructive testing in 1992, both from the University of Florence, Italy. She is currently an Associate Professor at the Department of Information Engineering, University of Siena, Italy. Her interests concern the development of measurement systems based on chemical and ultrasonic sensors and the development of automatic fault diagnosis systems. Recently, she has been involved in the study of random number generators based on chaotic maps.

Michele Gregorkiewitz holds a PhD in sciences from Technische Universität Darmstadt, Germany (1980). 1979 he collaborated as invited expert in the ionic conductivity group at Max-Planck-Institut für Festkörperforschung, Stuttgart, Germany. 1980-1992 he was research director for solid state chemistry and materials science at Instituto de Ciencia de Materiales, CSIC, Madrid, Spain. From 1994 he is professor of crystallography and materials science at Università di Siena. Current research interests include the crystallography and development of porous oxides exhibiting ionic and/or electronic conduction for applications in sensors, alternative energy and water desalination.

Marco Mugnaini received the Laurea degree in electronic engineering and the Ph.D. degree in reliability, availability, and logistics from the University of Florence, Florence, Italy, in 1999 and 2003, respectively.
Since 2003, he has been a Product Safety Engineer with General Electric Oil and Gas business, Florence, where he got his green belt certification. Since 2005, he has been an Assistant Professor with the Department of Information Engineering, University of Siena, Siena, Italy. His current interests include the development of measurement systems based on chemical sensors.

Roberto Spinicci has been an Associate Professor of chemistry at the Faculty of Engineering of the University of Florence, Florence, Italy. For many years he has been developing his research activity in the area of the heterogeneous catalytic reactions, focusing his attention mainly on the hydrocarbons and organic compounds oxidations and on the characterization of the investigated catalysts.

Valerio Vignoli received the laurea degree in electronic engineering from the University of Florence, Italy,in 1989, and the Ph.D. degree in nondestructive testing from the same university in 1994. Since 1997, he has been with the Department of Information Engineering, University of Siena, Siena, Italy, where he is currently an Associate Professor of electronics. His recent research interests include the design of data acquisition and processing systems based on chemical sensors and the design of analogand mixed-signal electronic circuits.

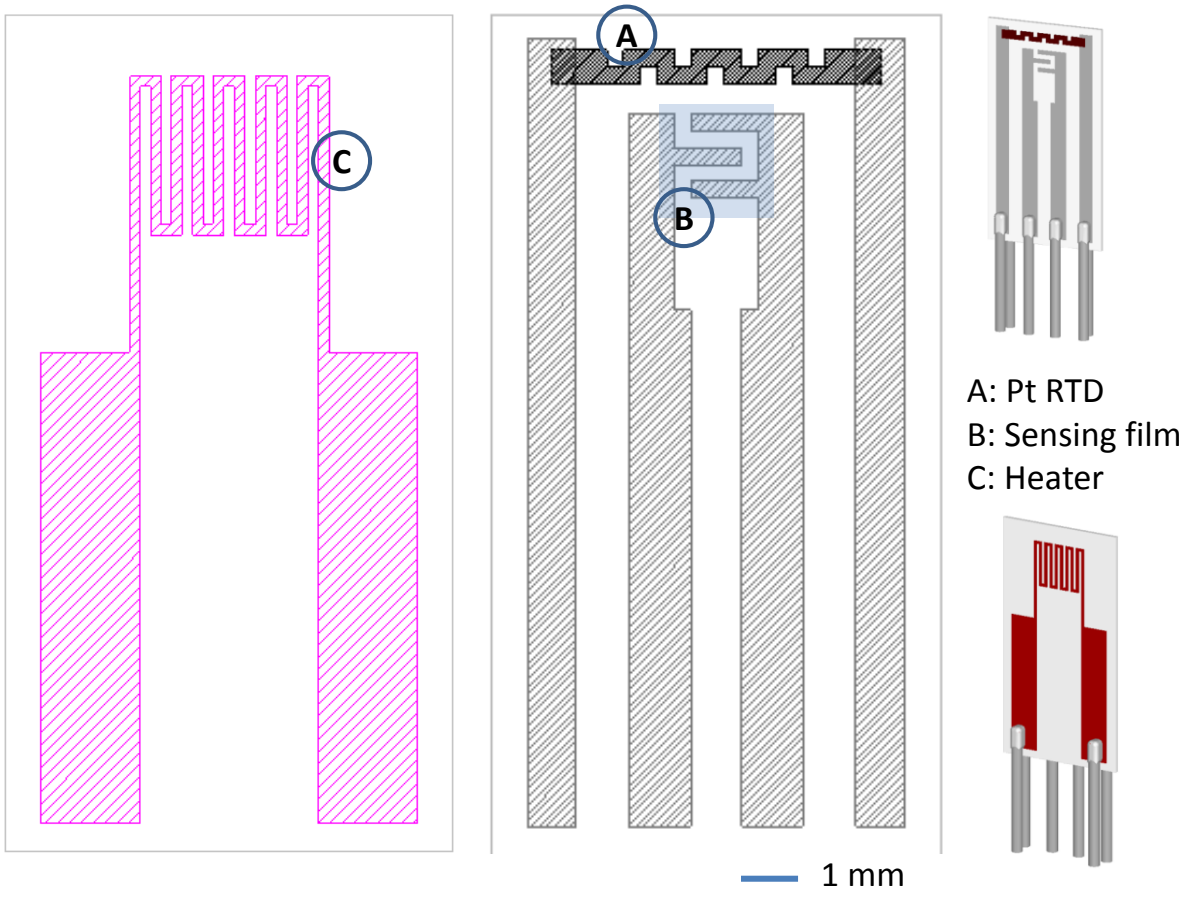

Figure 1. Structure of the sensor.

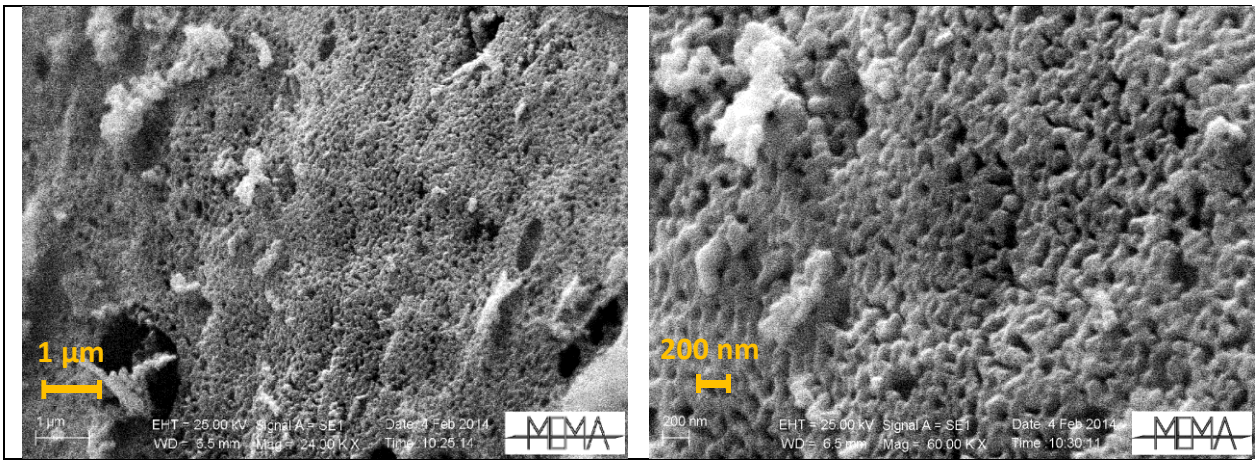

Figure 2. SEM micrographs of $YMnO_3$ obtained by self-combustion.

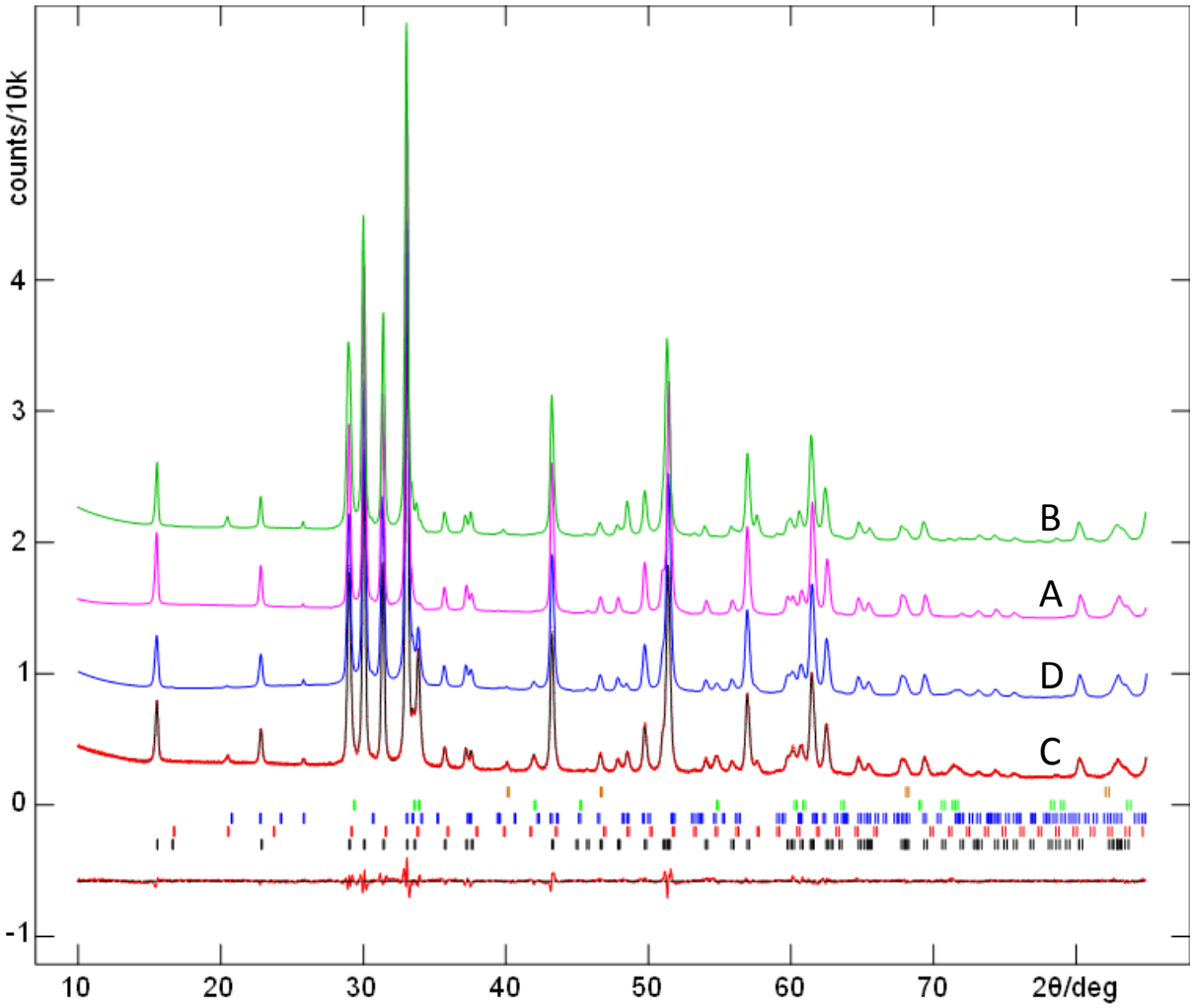

Figure 3. Powder X-ray diffraction patterns of some representative $YMnO_3$ materials. (A) $YMnO_3$, (B) $YMn_{0.9}O_3$, (C) $YMn_{0.9}Pd_{0.1}O_3$, (D) $YMn_{0.95}Pd_{0.05}O_3$. Dots (only for (C)) are observed intensities, lines are the calculated intensities obtained through Rietveld refinement, below their difference (for (C)). Ticks give reflection positions for hexagonal $YMnO_3$, Y_2O_3, orthorhombic $YMnO_3$, PdO and Pd, from bottom to top. Radiation is CuKα.

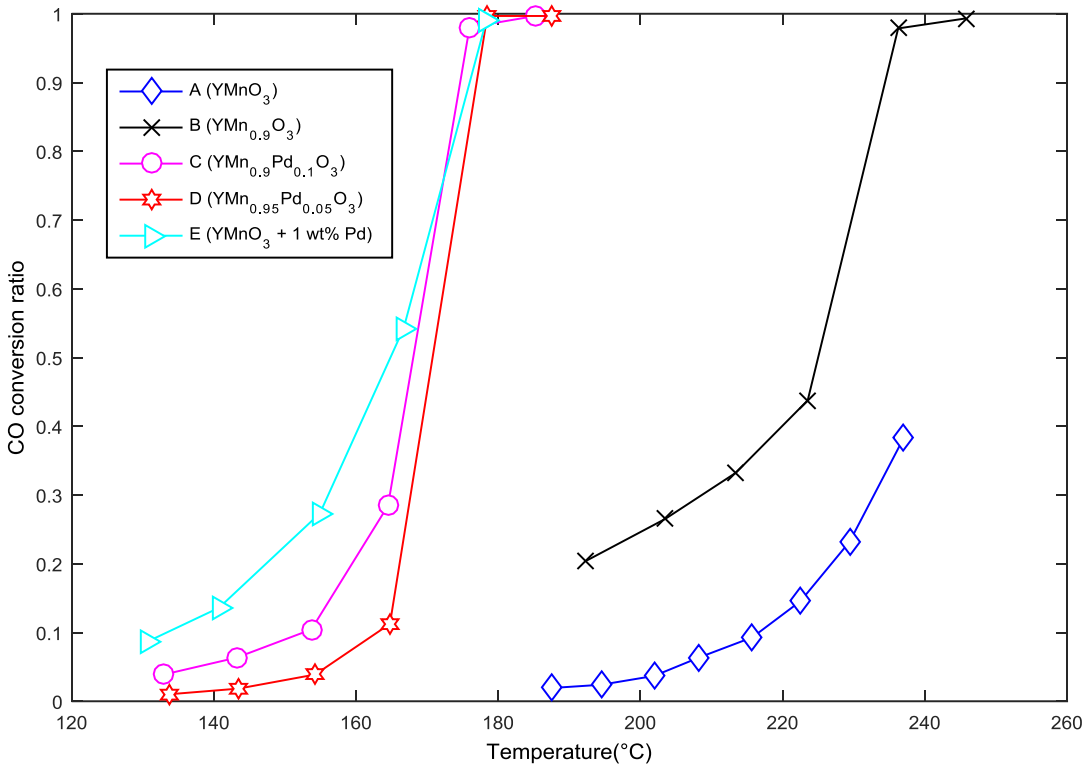

Figure 4. CO conversion results.

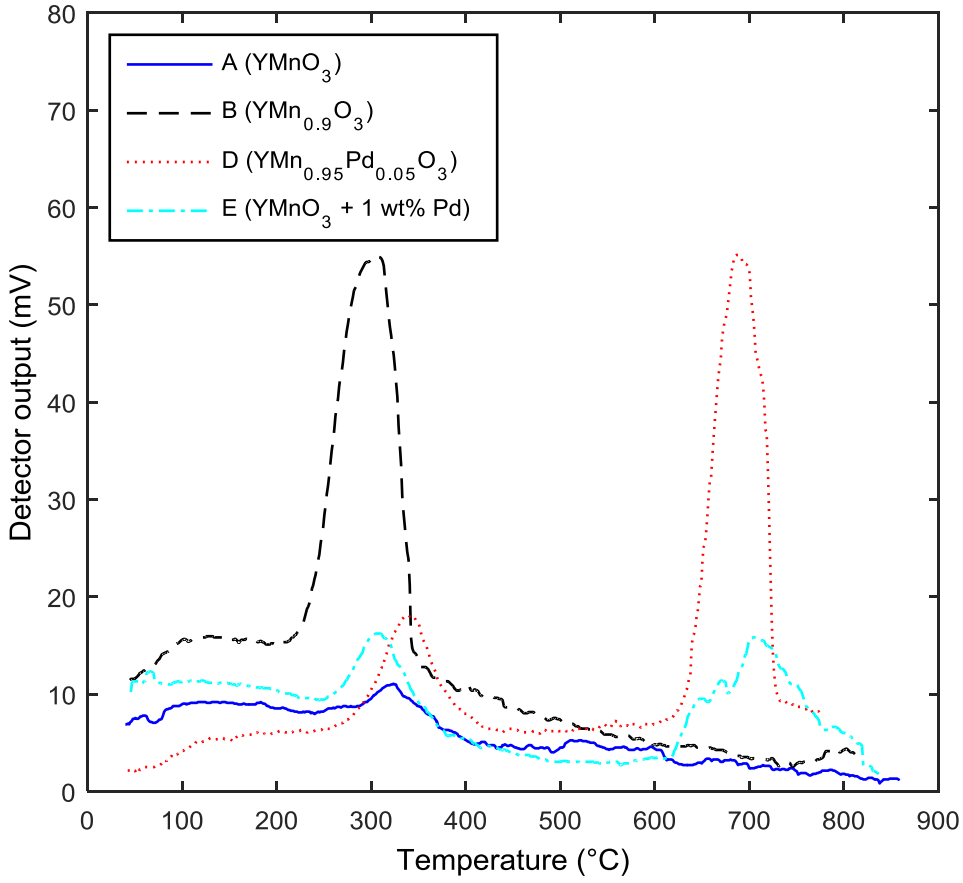

Figure 5. O_2-TPD experiments.

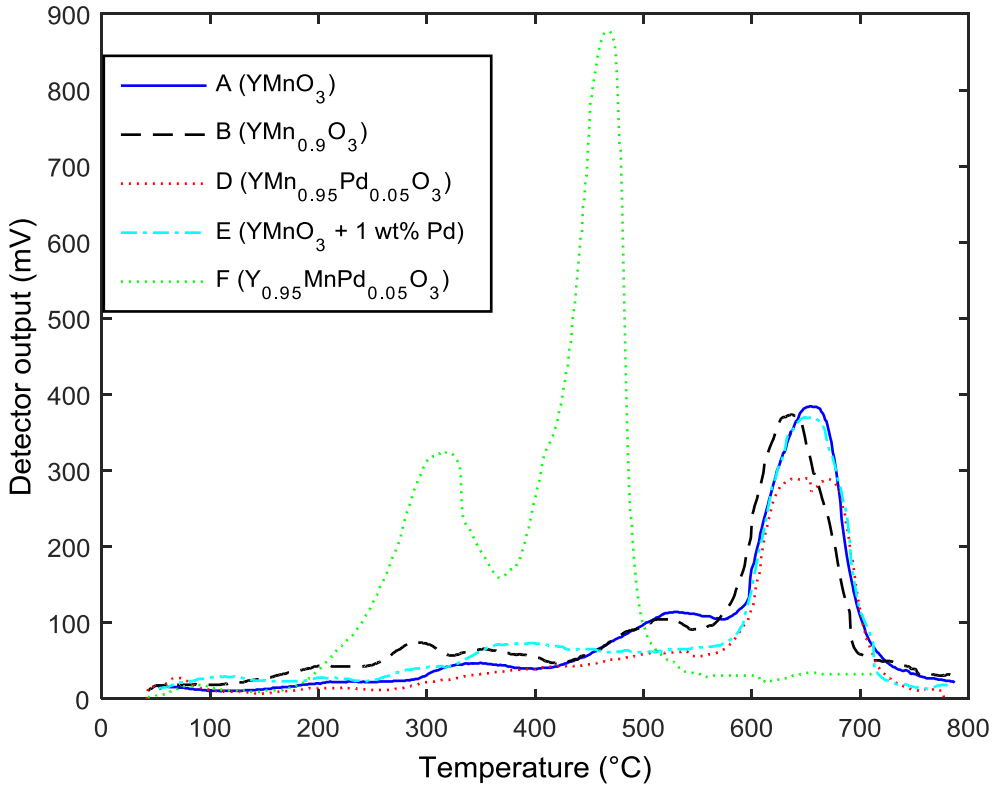

Figure 6. H_2-TPR experiments.

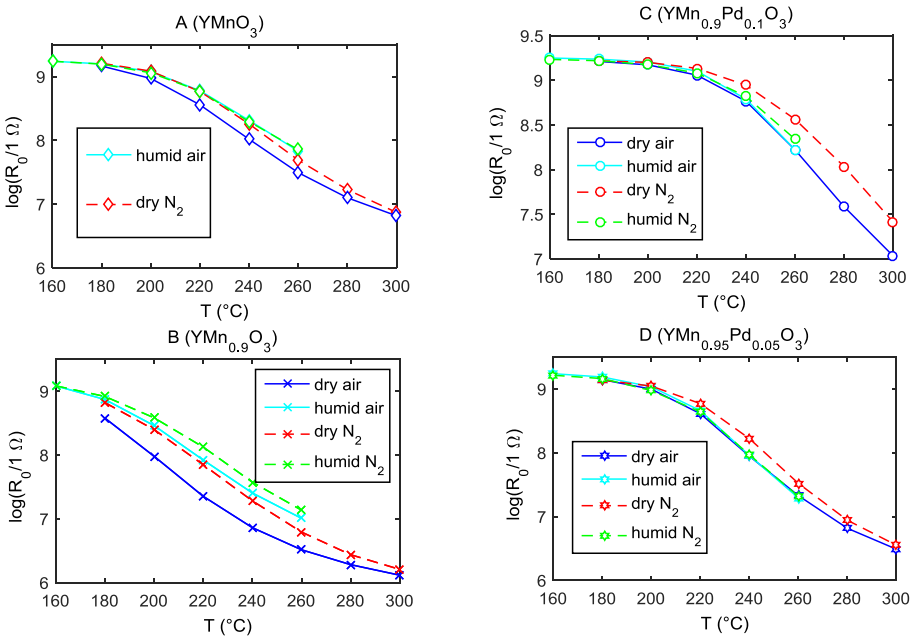

(a)

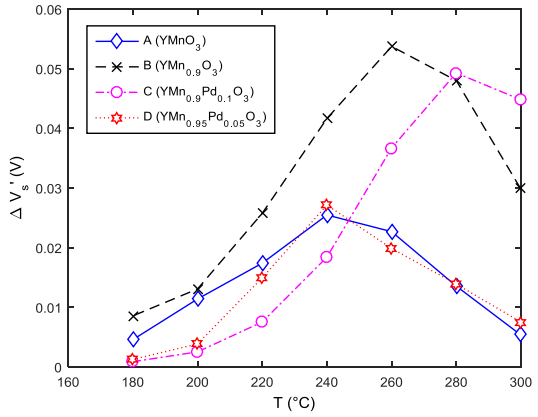

(b)

Figure 7. a) Base line resistance value for different materials in different environments. In humid air and N_2 RH is 25% @ 25°C (R_0 expressed in Ohms). b) Comparison of the estimated values of V_s in dry air and dry N_2 for the different materials (from data shown in figure 7a).

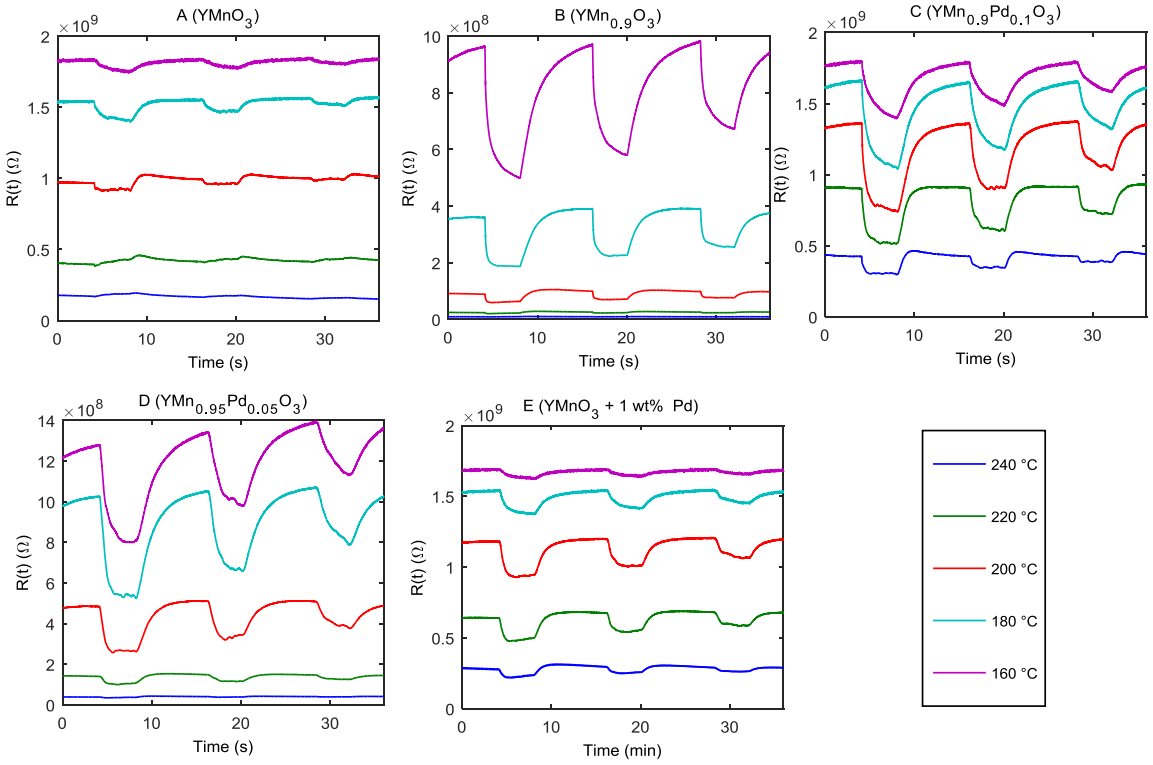

Figure 8. Resistance as a function of time in a flow of 200 mL/min of dry air and dry air/NO_2 mixtures for different sensor temperatures. Measurement protocol: 4 min - dry air, 4 min - dry air +23 ppm NO_2, 8 min - dry air, 4 min - dry air +12 ppm NO_2, 8 min - dry air, 4 min - dry air + 6 ppm NO_2, 4 min - dry air.

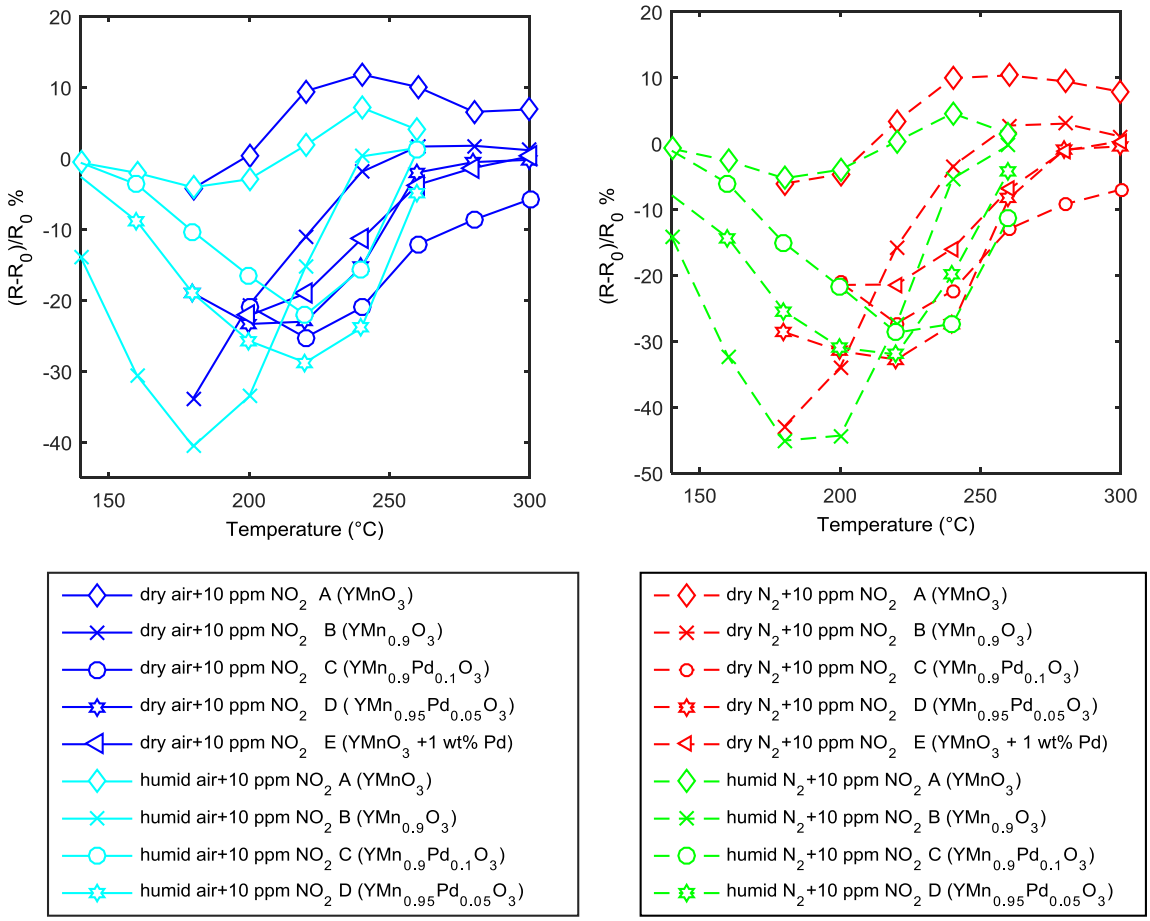

Figure 9. Response of the different materials as a function of the temperature. Total flow 200 mL/min. For humid mixtures RH=25% @25 °C.

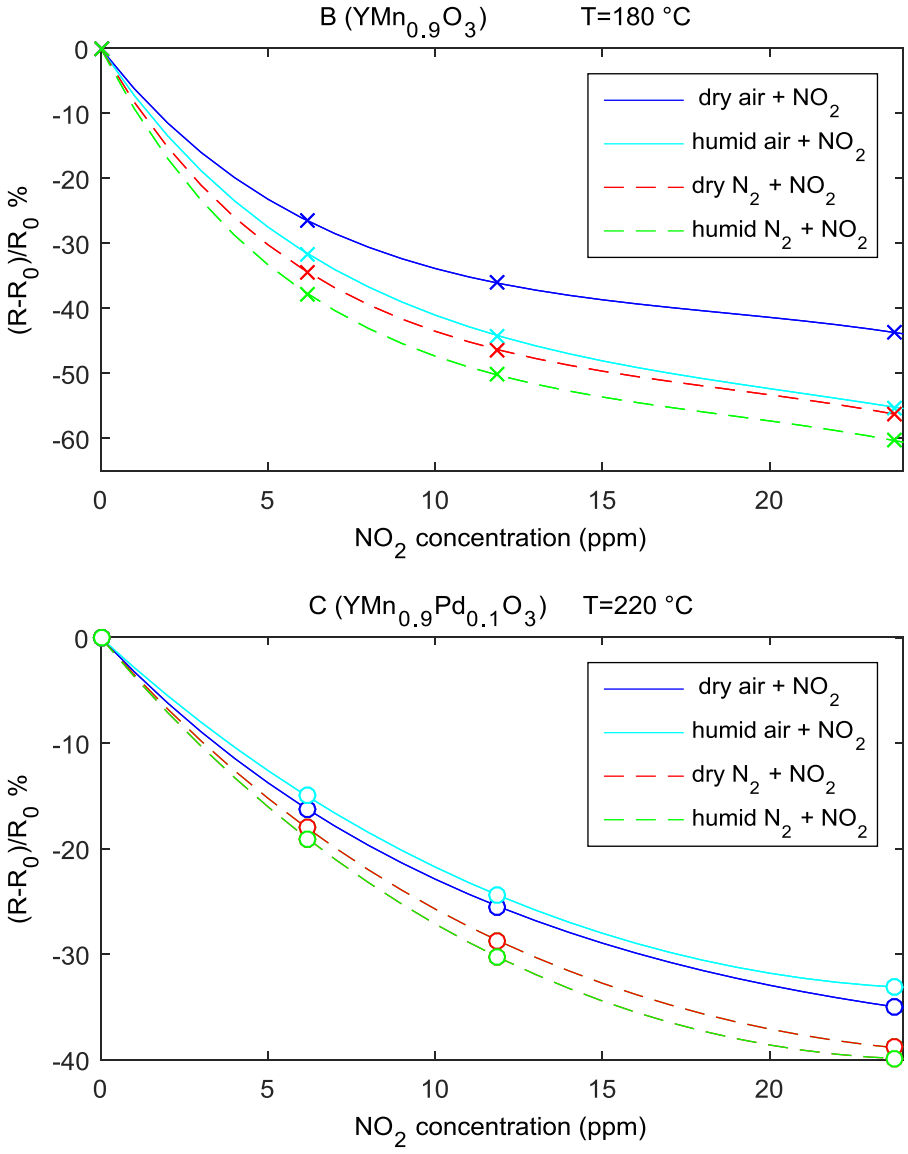

Figure 10. Response to NO_2 (air or N_2 as carrier gas, dry and humid conditions) as a function of NO_2 concentration at the optimum temperature for material B (180 °C) and C (200 °C). The data are obtained with the same protocol used in Figure 10.

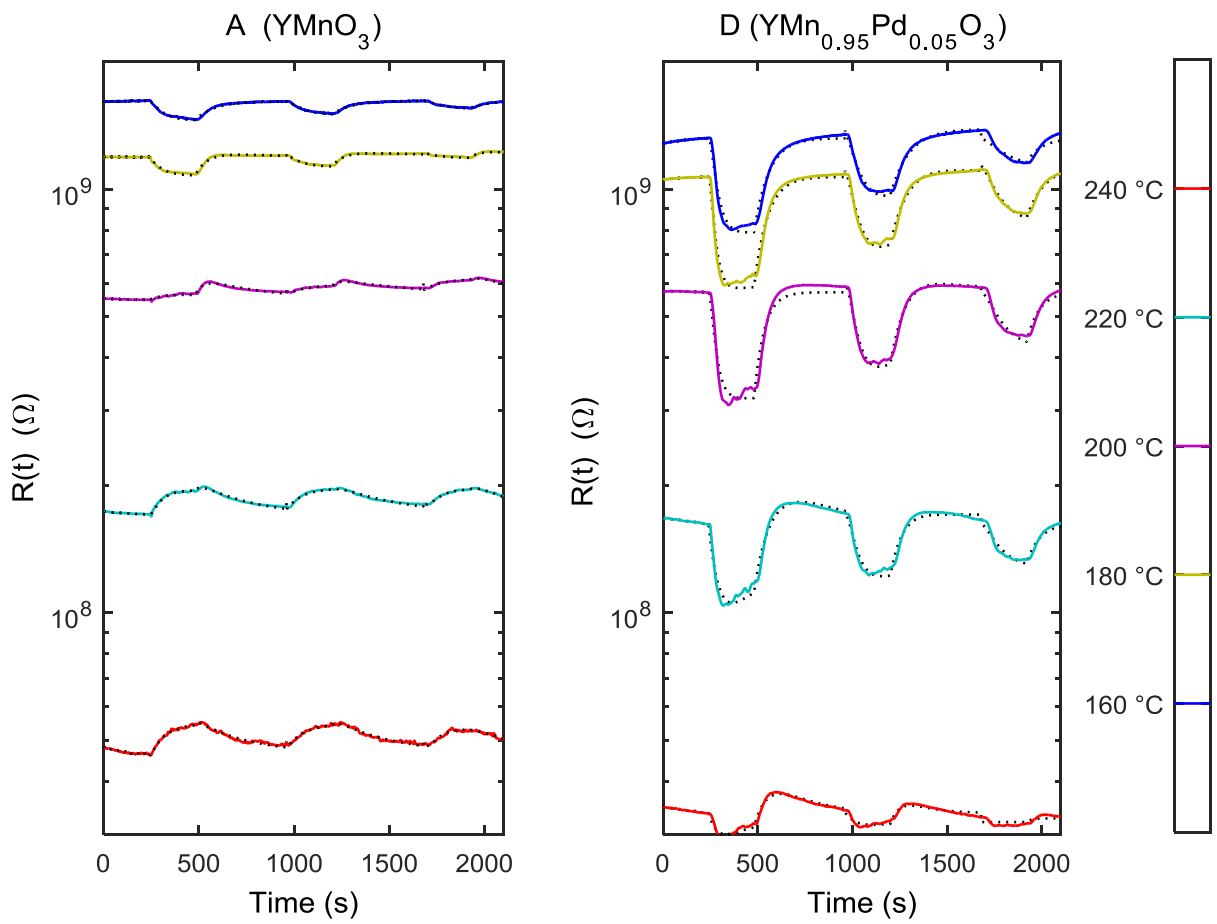

Figure 11. Resistance as a function of time. Left: stoichiometric material (A). Right $YMn_{0.95}Pd_{0.05}O_3$ (D). Colored continuous lines: experimental data. Dotted black lines: fitted data. Response to mixtures of nitrogen and NO_2. Measurement protocol: 4 min (240 s) - N_2, 4 min (240 s) - N_2 + 23 ppm NO_2, 8 min (480 s) - N_2, 4 min (240 s) - N_2 + 12 ppm NO_2, 8 min (480 s) - N_2, 4 min (240 s) - N_2 + 6 ppm NO_2, 4 min (240 s) - N_2.

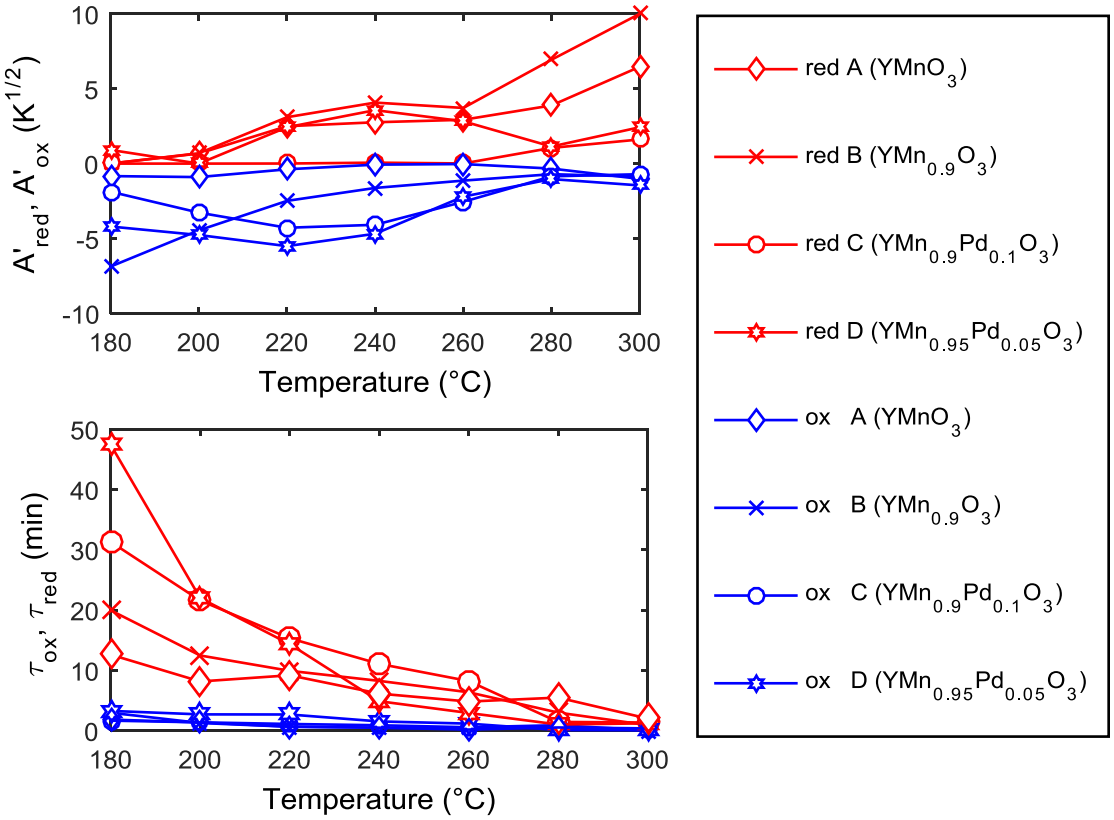

Figure 12. Parameters estimated for the model in eq. (14) for nitrogen and 23 ppm NO_2. $A_{red}' = qA_{red}/\sqrt{2\epsilon k p_b}$, and $A_{ox}' = qA_{ox}/\sqrt{2\epsilon k p_b}$.

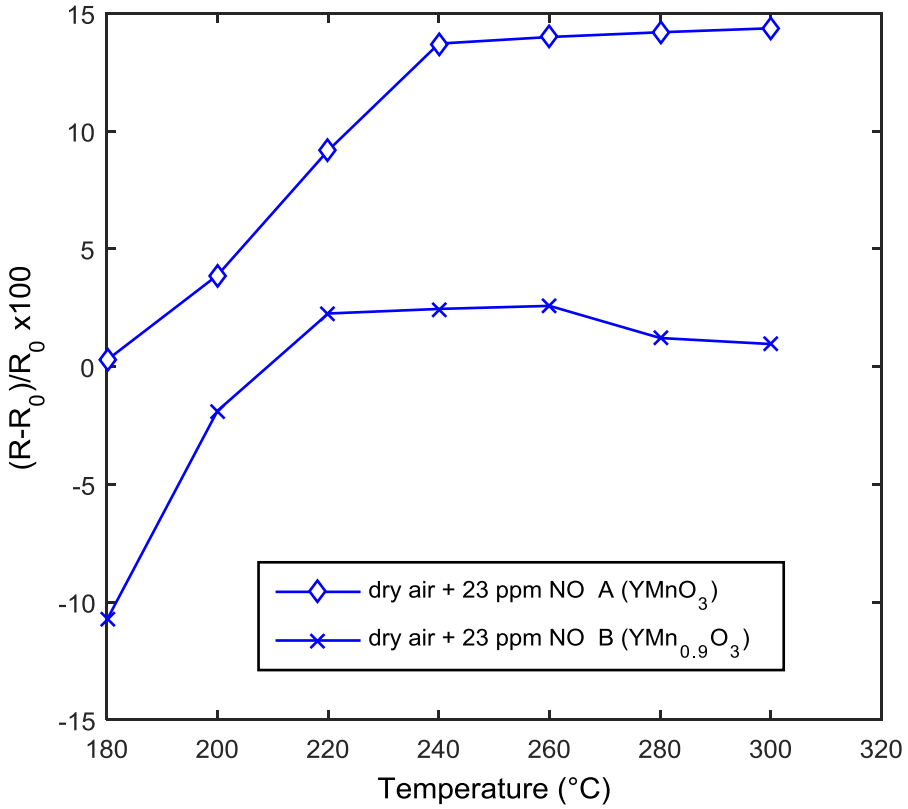

Figure 13. Response to NO and dry air as a function of temperature. The total flow is 200 mL/min.

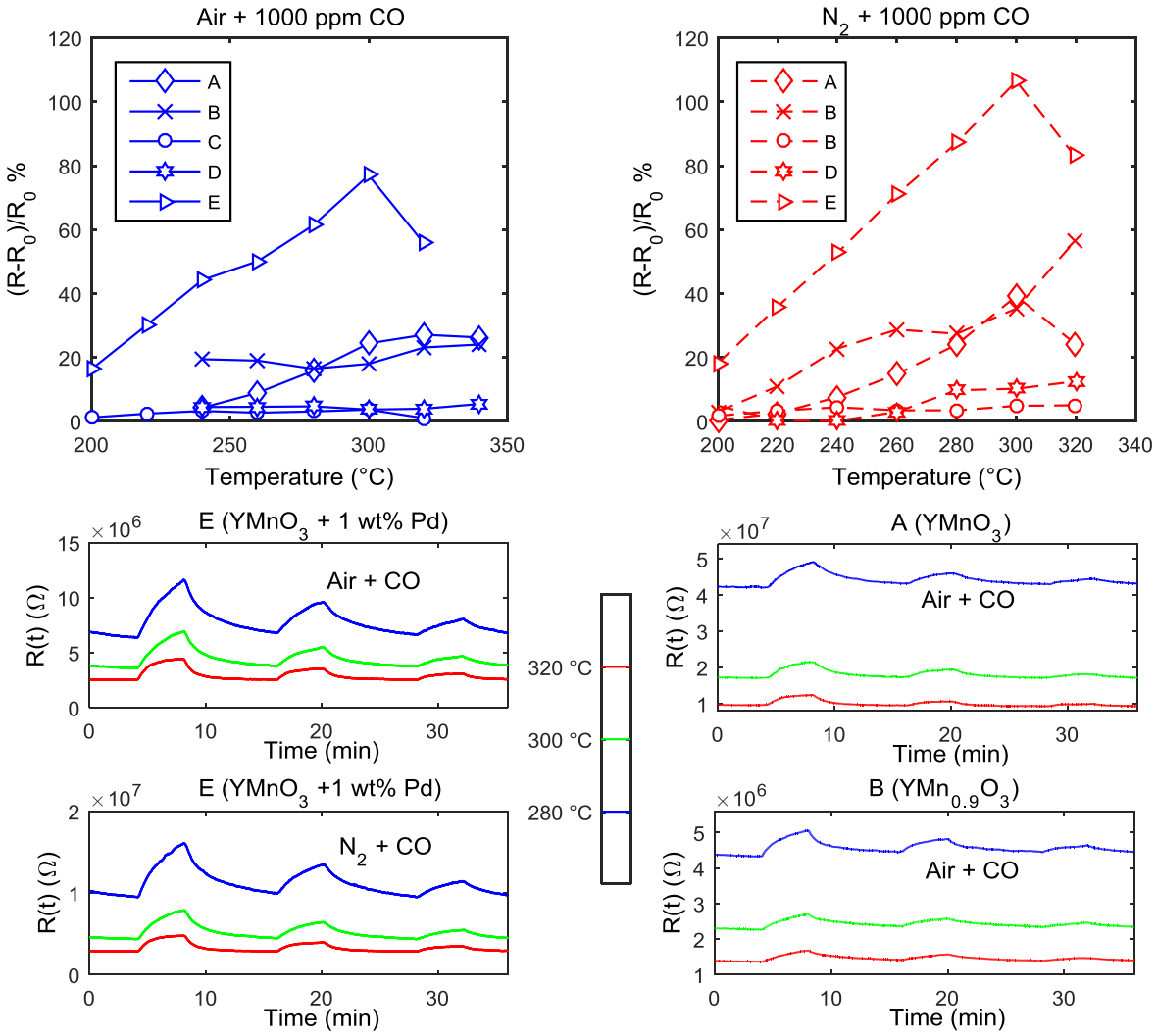

Figure 14. Experiments in mixtures of N_2 or air with CO. Measurement protocol: 4 min – dry air/N_2, 4 min - dry air/N_2 + 2000 ppm CO, 8 min - dry air/N_2, 4 min - dry air/N_2 + 1000 ppm CO, 8 min - dry air/N_2, 4 min - dry air/N_2 + 500 ppm CO, 4 min - dry air/N_2.

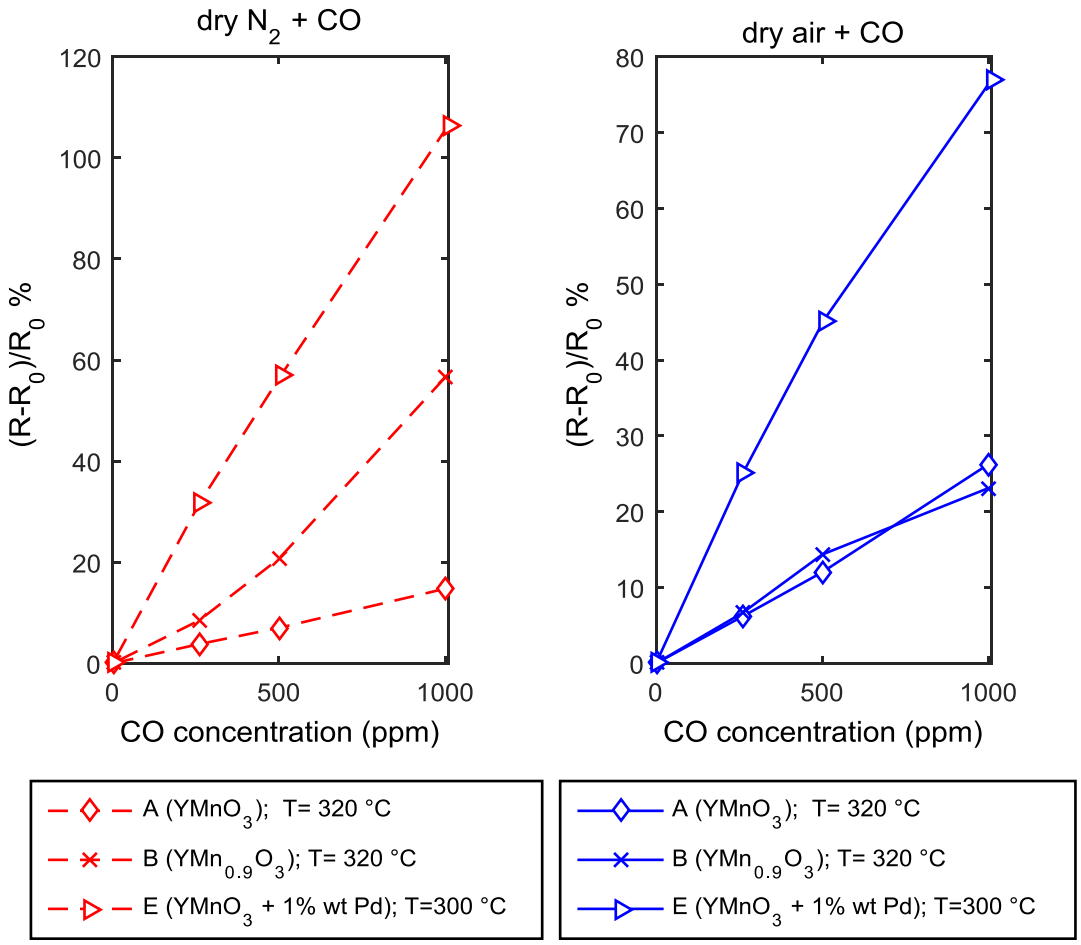

Figure 15. Response to CO (dry air or N_2 as carrier gas) as a function of CO concentration at the optimum temperature for material A (180 °C), B (320 °C), and E (300 °C). The data are obtained with the same protocol used in Figure 14.

Table I. List of the materials used for the experiments reported in the paper.

Material	Nominal Formula	Molar ratio in aqueous solution		Impregnation
		$Y(NO_3)_3 \cdot 6H_2O$: $Mn(NO_3)_2 \cdot 6H_2O$	$Pd(CH_3COO)_2$: $Y(NO_3)_3 \cdot 6H_2O$	
A	$YMnO_3$	1:1	0	no
B	$YMn_{0.9}O_3$	1:0.9	0	no
C	$YMn_{0.9}Pd_{0.1}O_3$	1:0.9	0.1:1	no
D	$YMn_{0.95}Pd_{0.05}O_3$	1:0.95	0.05:1	no
E	$YMnO_3$ +1 wt% Pd	1:1	0	Using 1% weight $Pd(CH_3COO)_2$.
F	$Y_{0.95}MnPd_{0.05}O_3$	0.95:1	0.05:0.95	no

Table II. Results of Rietveld refinement for pure, doped and defective $YMnO_3$ samples. Estimated standard deviations (in parentheses) refer to the last digits, *x* is the mass fraction of the component, the mol ratio is defined as $(2n[Y_2O_3]+n[PdO]+n[Pd])/(n[YMnO_3\ hex]+n[YMnO_3\ orth])$ where *n*[*i*] is the mol number of the *i*-th component, and SOF is the site occupation factor. Note that an understoichiometry of metals is formally equivalent to an overstoichiometry of oxygen. Refinement of SOF(metal) was preferred as it gives, at the same time, an opportunity to check the Y/Mn ratio.

material		A ($YMnO_3$)	B ($YMn_{0.9}O_3$)	C ($YMn_{0.9}Pd_{0.1}O_3$)	D ($YMn_{0.95}Pd_{0.05}O_3$)
error indices					
χ^2		3.86	3.85	3.09	4.71
R_p		0.023	0.024	0.022	0.026
$R(F^2)$		0.033	0.045	0.032	0.033
composition					
$YMnO_3$ hex	*x*	0.99027(7)	0.8936(9)	0.8682(8)	0.9368(6)
Y_2O_3	*x*	0.0003(3)	0.0821(8)	0.0481(7)	0.0150(7)
$YMnO_3$ orthorh	*x*	0.0095(7)	0.0243(11)	0.0152(10)	0.0160(8)
PdO	*x*	-	-	0.0655(5)	0.0312(4)
Pd	*x*	-	-	0.0030(2)	0.0009(2)
mol ratio (Y+Pd)/$YMnO_3$	obs calc	$<5\cdot10^{-4}$ 0	0.15 0.11	0.21 0.22	0.08 0.11
unit cell, structure					
$YMnO_3$ hex	*a*/Å	6.14640(9)	6.1620(1)	6.1560(1)	6.1531(1)
	c/Å	11.3939(2)	11.3835(3)	11.3954(2)	11.3975(3)
	V/Å^3	372.8	374.3	374.0	373.7
	c/a	1.8538	1.8474	1.8511	1.8523
SOF	Y1	0.954(3)	1.048(4)	1.001(3)	0.986(4)
SOF	Y2	0.962(3)	1.056(4)	1.009(3)	0.994(4)
SOF	Mn	0.963(4)	1.089(5)	1.029(4)	1.014(5)
Y_2O_3	*a*/Å	10.6052(fix)	10.6032(4)	10.6052(5)	10.618(2)
$YMnO_3$ orthorh	*a*/Å	5.264(1)	5.259(1)	5.262(1)	5.258(2)
	b/Å	5.825(2)	5.836(1)	5.832(2)	5.830(2)

Table III. Parameter R_A of the different materials.

Material	Nominal Formula	Model parameter R_A (Ω)
A	$YMnO_3$	1.42×10^5
B	$YMn_{0.9}O_3$	4.54×10^4
C	$YMn_{0.9}Pd_{0.1}O3$	3.77×10^5
D	$YMn_{0.95}Pd_{0.05}O_3$	3.06×10^5